ELSEVIER

J. Non-Newtonian Fluid Mech. 108 (2002) 363–409

Journal of Non-Newtonian Fluid Mechanics

www.elsevier.com/locate/jnnfm

Free surface flows of polymer solutions with models based on the conformation tensor

Matteo Pasquali*, L.E. Scriven

Coating Process Fundamentals Program, Department of Chemical Engineering and Materials Science, Center for Interfacial Engineering, University of Minnesota Supercomputing Institute, University of Minnesota, Minneapolis, MN 55455, USA

Abstract

A computational method is presented for analyzing free surface flows of polymer solutions with the conformation tensor. It combines methods of computing Newtonian free surface flows [J. Comp. Phys. 99 (1992) 39; V.F. deAlmeida, Gas–Liquid Counterflow Through Constricted Passages, Ph.D. thesis, University of Minnesota, Minneapolis, MN, 1995 (Available from UMI, Ann Arbor, MI, order number 9615160); J. Comp. Phys. 125 (1996) 83] and viscoelastic flows [J. Non-Newtonian Fluid Mech. 60 (1995) 27; J. Non-Newtonian Fluid Mech. 59 (1995) 215]. Modifications are introduced to compute a traceless velocity gradient, to impose inflow boundary conditions on the conformation tensor that are independent of the specific model adopted, and to include traction boundary conditions at free surfaces and open boundaries.

A new method is presented for deriving and coding the entries of the analytical Jacobian for Newton's method by keeping the derivatives of the finite element weighted residual equations with respect to the finite element basis functions in their natural vector and tensor forms, and then by mapping such vectors and tensors into the elemental Jacobian matrix. A new definition of extensional and shear flow is presented that is based on projecting the rate of strain tensor onto the principal basis defined by the conformation tensor.

The method is validated with two benchmark problems: flow around a cylinder in a channel, and flow under the downstream section of a slot or knife coater. Regions of molecular stretch—determined by monitoring the eigenvalues of the conformation tensor—and molecular extension and shear rate—determined by projecting the rate of strain dyadic onto the eigenvectors of the conformation tensor—are shown in the flow around a cylinder of an Oldroyd-B liquid.

The free surface coating flow between a moving rigid boundary and a parallel static solid boundary from which a free surface detaches is analyzed with several models of dilute and semidilute solutions of polymer of varying degree of stiffness based on the conformation tensor approach [J. Non-Newtonian Fluid Mech. 23 (1987) 271; A.N. Beris, B.J. Edwards, Thermodynamics of Flowing Systems with Internal Microstructure, 1st ed., Oxford University Press, Oxford, 1994; J. Rheol. 38 (1994) 769; M. Pasquali, Polymer Molecules in Free Surface Coating Flows, Ph.D. thesis, University of Minnesota, Minneapolis, MN, 2000 (Available from UMI, Ann Arbor, MI, order number 9963019)].

---

* Corresponding author. Present address: Chemical Engineering Department, Rice University, MS 362, P.O. Box 1892, Houston, TX 77251-1892, USA.

E-mail addresses: mp@rice.edu (M. Pasquali), pjensen@cems.umn.edu (L.E. Scriven).

PII: S0377-0257(02)00138-6

Although the boundary conditions at the static contact line introduce a singularity, that singularity does not affect the computation of flows at high Weissenberg number when a recirculation is present under the static boundary. In this case, a steep layer of molecular stretch develops under the free surface downstream of the stagnation point. Here the polymer aligns with its principal stretching axis parallel to the free surface. When the recirculation is absent, the singularity at the contact line strongly affects the computed velocity gradient, and the computations fail at moderate Weissenberg number irrespective of the polymer model and of whether the polymer is affecting the flow or not.

Keywords: Free surface flows; Polymer solutions; Conformation tensor; Viscoelastic flows; Flow type classification; Finite elements

1. Introduction

Free surface flows and free boundary problems arise when one or more layers of liquids flow together, possibly meeting a gas at one or more interfaces, and possibly interacting with a deformable elastic solid at other interfaces. Such problems abound in coating (e.g. slot coating, deformable roll coating), polymer processing (e.g. extrusion, calendering), cell engineering (e.g. deformation of blood cells), hemodynamics (blood flow in arteries), and biomechanics and tissue engineering (lubrication flow in articular joints, carthilage deformation).

The mathematical modeling of free surface flows requires solving free boundary problems, i.e. problems where the domain of definition of the differential equations describing the flow is unknown and its location must be part of the solution of the problem. Open flow boundaries are often present where the liquid enters or exits the flow domain; approximate boundary conditions are imposed there that are not dictated by the physics of the problem, but by the need of truncating the computational domain, and the sensitivity of the flow computations to the location of the open boundaries must be assessed and reduced to an acceptable level.

The methods used to compute Newtonian free surface flows are also applicable to viscoelastic free surface flows. Different ways of handling free surface flows are discussed in detail by Kistler and Scriven [10,11], Christodoulou and Scriven [1], Christodoulou [12], deAlmeida [2,13] and Sackinger et al. [3]. Such methods have been extended successfully to elastohydrodynamics problems, where a flowing Newtonian liquid interacts with a deformable elastic solid at common boundaries [14–16].

Computational methods to solve viscoelastic flows are still an active area of research, and several methods of solving the partial differential equations of such flows have been proposed in recent years (see [17] for a recent review). The method used here is a slight modification of the discrete elastico-viscous split stress, independent velocity gradient interpolation, streamline upwind Petrov–Galerkin (DEVSS-G/SUPG) [5], one of the youngest members of the family of methods of weighted residuals with finite element basis functions that originated in the elastico-viscous split stress (EVSS) [18]. The DEVSS-G/SUPG method and its variants are convergent and accurate at low and moderate values of the Weissenberg number [4,5,19–21].

The set of non-linear algebraic equations for the finite element basis functions that arises from applying the method of weighted residuals to the conservation equations of mass, momentum, and polymer conformation, together with the elliptic mesh generation equations and the appropriate boundary conditions, is solved by Newton's method with analytical Jacobian and first-order arclength continuation in parameter space [22].

Because the number of scalar differential equations to solve is high (12 or 13 for two-dimensional flows, 22 for three-dimensional flows), a large number of analytical derivatives must be calculated to compute the analytical Jacobian. To reduce the number of analytical derivatives, the coefficients of the finite element basis functions and the residual equations residuals of the elliptic mesh generation are kept in their natural vector or tensor form. The number of equations and unknowns is thereby reduced to 5 and the number of analytical derivatives needed drops accordingly, although these derivatives are tensor-valued.

The residual equations and Jacobian entries depend on the particular constitutive form of the free energy and the generation terms in the transport equation of conformation. A general method is developed of writing computer code that reflects the tensorial nature of the equations and unknown basis function coefficients, and that is independent of the particular constitutive choices, provided that the constitutive equation belongs to the conformation tensor family [6–9], so that only few short user-specified routines must be changed to solve free surface flows of polymer solutions with different constitutive equations. To make the method fully general, a new way of imposing inflow boundary conditions on the conformation tensor (or elastic stress) is introduced that is independent of the choice of constitutive model.

The theory and computational method are applied to analyze coating flows of polymer solutions, for which there are very few results based on simplified one-dimensional analysis [23], asymptotic expansions [24], or early attempts at solving the two-dimensional free surface flow problem with the EVSS method [25]. In coating operations, the degree of stiffness of the polymer molecules dissolved in the coating liquid ranges from low, as in aqueous solutions of polyethylene oxide, to high, as in solutions of xanthan [26], and may depend on the type of solvent surrounding the molecules, and on the concentration of polymer. Polymer concentrations range from few parts per million, as in some specialized precision coating operations, to almost pure polymer, as in hot-melt coating of low-molecular weight adhesives. Studying how different types of polymer molecules behave in coating flows in different concentration regimes is therefore important.

The interaction of flow and polymer microstructure is analyzed in the free surface flow between a moving rigid boundary and a parallel static solid boundary from which a free surface detaches (Fig. 6). This free surface flow is a prototype coating flow; it is the downstream section, or tail-end, of a slot coater, if the flow rate through the inflow boundary is fixed, i.e. the flow is premetered; and it is the downstream section of a knife coater, if the pressure difference between the inflow section and the gas outside the free surface is fixed and the flow rate is allowed to change, i.e. the flow is self-metering.

The solutions considered are infinitely dilute, dilute, and semidilute in polymer, none of them entangled, so that their salient microstructural features can be modeled with a single variable, the conformation dyadic, or second-order tensor [6–9]. The polymer molecules are extensible, semiextensible, and rigid linear molecules. The simple models used to capture these molecular characteristics in the equation of change of the conformation dyadic are described in Section 3 below.

2. Elliptic mesh generation/domain deformation

To compute a free surface flow, the unknown flow domain (physical domain) is mapped into a fixed reference domain (computational domain). Common ways of constructing the mapping are the method of spines [10,27]; the elliptic mesh generation method [1,12], where the mapping is the solution of an elliptic differential equation; and the domain deformation method [2,3,13], where the mapping is

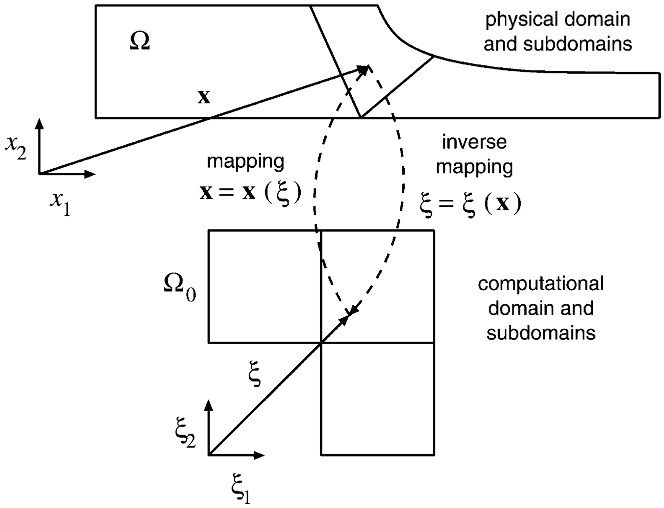

Fig. 1. Mapping of the physical domain into the computational domain.

computed by solving the equilibrium equations of a hypothetical elastic solid whose stress-free state is the computational domain, and whose deformed state is the physical domain. The version of the elliptic mesh generation method summarized here is described in detail by deSantos [28].

A complex physical domain is subdivided into quadrangular subdomains, which are mapped into separate subdomains of the computational domain (Fig. 1). Position in the physical domain Ω is denoted by $\boldsymbol{x}$, and position in the computational domain Ω_0 by $\boldsymbol{\xi}$. The direct mapping (computational domain → physical domain) is given by the function $\boldsymbol{x} = \boldsymbol{x}(\boldsymbol{\xi})$, and the inverse mapping (physical → computational domain) is represented by the function $\boldsymbol{\xi} = \boldsymbol{\xi}(\boldsymbol{x})$. The mapping must be invertible and must map boundaries of the computational subdomains into boundaries of the physical subdomains.

In the elliptic mesh generation method, the inverse mapping is taken to satisfy the elliptic differential equation

$$\nabla \cdot \tilde{\boldsymbol{D}} \cdot \nabla \boldsymbol{\xi} = 0 \tag{1}$$

where $\nabla \equiv \partial/\partial \boldsymbol{x}$ denotes differentiation in physical space, and the dyadic $\tilde{\boldsymbol{D}}$ controls the spacing of the coordinate lines [29]. In the domain deformation method, the inverse mapping is taken to satisfy the inertialess momentum balance equation of a fictitious solid body:

$$\nabla \cdot \boldsymbol{S} = 0 \tag{2}$$

where $\boldsymbol{S}$ is the Cauchy stress of the pseudo-solid; it must be related to the gradient of the deformation mapping $\boldsymbol{F} \equiv \partial \boldsymbol{x}/\partial \boldsymbol{\xi}$ through a constitutive equation, e.g. a pseudo-Hookean constitutive equation [3]:

$$\boldsymbol{S} = 3\lambda_s((\det \boldsymbol{F})^{1/3} - 1)\boldsymbol{I} + \mu_s(\boldsymbol{I} - \boldsymbol{F}^{\mathrm{T}} \cdot \boldsymbol{F}) \tag{3}$$

more general constitutive equations are discussed by deAlmeida [2,13]. Hereafter, the computational method is developed in the context of elliptic mesh generation techniques without loss of generality.

The direct mapping $\boldsymbol{x} = \boldsymbol{x}(\boldsymbol{\xi})$ is built by using finite element basis functions $\varphi_{\boldsymbol{x}}^{\alpha}(\boldsymbol{\xi})$,

$$\boldsymbol{x} = \boldsymbol{x}^{\alpha}\varphi_{\boldsymbol{x}}^{\alpha}(\boldsymbol{\xi}), \qquad x_i = x_i^{\alpha}\varphi_{\boldsymbol{x}}^{\alpha}(\boldsymbol{\xi}) \tag{4}$$

where $\boldsymbol{x}^\alpha$ is the set of unknown coefficients, and the index i denotes direction in physical space. Einstein's summation convention over repeated Greek or italic indices is used hereafter. The subscript on the basis function denotes the variable that is approximated with that basis function; the Greek index identifies each basis function in the basis set. The same basis functions are used for the components of the same variable. The italic subscript or subscripts on the basis function coefficients represent vector or tensor components in space, and the Greek superscripts identify each coefficient. The physical components of the approximated value of a variable are identified with italic subscripts and no superscript.

Boundary conditions used to solve Eq. (1) are: (1) *prescribed angle*: the angle θ between the coordinate line ξ_i and the boundary is assigned, $\boldsymbol{n} \cdot \nabla\xi_i = |\nabla\xi_i| \cos\theta$, $i = 1$ or 2; (2) *slide over boundary*: the nodes are free to slide on a line whose equation is $f(\boldsymbol{x}) = 0$; (3) *fixed nodes*: the location of the nodes on the boundary is fixed, $\boldsymbol{x}^\alpha = \bar{\boldsymbol{x}}^\alpha$, where $\bar{\boldsymbol{x}}^\alpha$ is the pre-assigned position of node α; (4) *prescribed nodal distribution*: the nodes are distributed on the boundary of the physical domain according to a function g that controls their spacing, $\xi_i = g(s)$, $i = 1$ or 2; (5) *no-penetration* (*kinematic*): the liquid cannot cross a free surface, $\boldsymbol{n} \cdot \boldsymbol{v} = 0$.

3. Transport equations

The transport equations of mass, momentum, and conformation in a steady, isothermal, incompressible, non-diffusing flow of a non-entangled polymer solution are [9]:

$$0 = \nabla \cdot \boldsymbol{v} \tag{5}$$

$$0 = \rho\boldsymbol{v} \cdot \nabla\boldsymbol{v} - \nabla \cdot \boldsymbol{T} - \nabla\Theta \tag{6}$$

$$\begin{aligned} 0 = {} & \boldsymbol{v} \cdot \nabla\boldsymbol{M} - 2\xi\left(\frac{\boldsymbol{D} : \boldsymbol{M}}{\boldsymbol{I} : \boldsymbol{M}}\boldsymbol{M}\right) \\ & - \zeta\left(\boldsymbol{M} \cdot \boldsymbol{D} + \boldsymbol{D} \cdot \boldsymbol{M} - 2\frac{\boldsymbol{D} : \boldsymbol{M}}{\boldsymbol{I} : \boldsymbol{M}}\boldsymbol{M}\right) - \boldsymbol{M} \cdot \boldsymbol{W} - \boldsymbol{W}^{\mathrm{T}} \cdot \boldsymbol{M} + \frac{1}{\lambda}(g_0\boldsymbol{I} + g_1\boldsymbol{M} + g_2\boldsymbol{M}^2) \end{aligned} \tag{7}$$

where $\boldsymbol{v}$ is the liquid's velocity, ρ the liquid's density, $\boldsymbol{T}$ the stress tensor (Cauchy), Θ the potential of the body forces per unit volume, $\boldsymbol{M}$ the dimensionless conformation dyadic, $\boldsymbol{D}$ the rate of strain, $\boldsymbol{W}$ the vorticity dyadic, and λ is the characteristic relaxation time of the polymer. The constitutive function $\xi(\boldsymbol{M})$ represents the resistance of the polymer segments to stretching along their backbone, $\zeta(\boldsymbol{M})$ represents the resistance of the segments to relative rotation with respect to neighbors, and $g_0(\boldsymbol{M})$, $g_1(\boldsymbol{M})$, $g_2(\boldsymbol{M})$ define the rate of relaxation of the polymer segments. The dimensionless conformation dyadic is used because the number of polymer segments per unit volume is constant if the polymer solution is not entangled and if chemical reactions and polymer degradation are absent. The dimensionless conformation dyadic is related to the dimensional conformation dyadic $\hat{\boldsymbol{M}} \equiv c_p\langle\boldsymbol{rr}\rangle$ by the relation $\boldsymbol{M} \equiv 3/(c_pNl^2)\hat{\boldsymbol{M}} = 3/(Nl^2)\langle\boldsymbol{rr}\rangle$ where c_p is the number of polymer molecules per unit mass, N is the number of Kuhn steps per polymer segment [30], l is the length of a Kuhn step, $\boldsymbol{r}$ is the end-to-end connector of a segment, and $\langle\cdot\rangle$ denotes average over the distribution of orientations of segments. At equilibrium $\boldsymbol{M} = \boldsymbol{I}$.

The stress dyadic $\boldsymbol{T}$ is split into isotropic, viscous, and elastic components,

$$\boldsymbol{T} = -p\boldsymbol{I} + \boldsymbol{\tau} + \boldsymbol{\sigma} \tag{8}$$

where the pressure p is constitutively indeterminate because the liquid is incompressible, the viscous stress $\boldsymbol{\tau}$ obeys Newton's law of viscosity,

$$\boldsymbol{\tau} = 2\mu \boldsymbol{D} \tag{9}$$

and the elastic stress $\boldsymbol{\sigma}$ follows the constitutive relation [9]:

$$\boldsymbol{\sigma} = 2(\xi - \zeta)\frac{\boldsymbol{M}}{\boldsymbol{I}:\boldsymbol{M}}\boldsymbol{M} : \frac{\partial a}{\partial \boldsymbol{M}} + 2\zeta \boldsymbol{M} \cdot \frac{\partial a}{\partial \boldsymbol{M}} \tag{10}$$

where $a(T, \boldsymbol{M})$ is the Helmholtz free energy per unit volume.

A particular form of the constitutive functions $\xi(\boldsymbol{M})$, $\zeta(\boldsymbol{M})$, $g_0(\boldsymbol{M})$, $g_1(\boldsymbol{M})$, $g_2(\boldsymbol{M})$, and $a(T, \boldsymbol{M})$ must be chosen to compute the flow of a particular polymeric liquid. However, the computational method and computer programs needed to perform the calculations are independent of the specific choice of constitutive functions, and they are developed in the general case. The different models of polymer behavior used to analyze the free surface flow under a static edge are outlined here. These models may be crude approximations to how real polymer chains behave, but they do capture at least qualitatively some essential features and differences between polymers of different type.

3.1. *Affinely deforming, infinitely extensible molecules (Gaussian)*

Two hypotheses enter this model: (1) the molecules follow imposed larger-scale deformations affinely: $\xi \equiv \zeta \equiv 1$; the rate of relaxation of the molecules is a linear function of the distance of the dimensionless conformation tensor $\boldsymbol{M}$ from its equilibrium value $\boldsymbol{I}$: $g_0 \equiv -1$, $g_1 \equiv 1$, $g_2 \equiv 0$. With these hypotheses, the evolution equation of the dimensionless conformation dyadic is

$$\dot{\boldsymbol{M}} \equiv \frac{\partial \boldsymbol{M}}{\partial t} + \boldsymbol{v} \cdot \nabla \boldsymbol{M} = \nabla \boldsymbol{v}^{\mathrm{T}} \cdot \boldsymbol{M} + \boldsymbol{M} \cdot \nabla \boldsymbol{v} - \frac{1}{\lambda}(\boldsymbol{M} - \boldsymbol{I}) \tag{11}$$

Eq. (11) yields the Upper Convected Maxwell model if the Helmholtz free energy per unit volume of the liquid depends linearly on the trace of the conformation dyadic, $a \equiv (G/2)\mathrm{Tr}\,\boldsymbol{M}$, and there is no viscous stress; it yields the Oldroyd-B model, if the stress has both an elastic and a viscous components.

The ratio of the volume pervaded by the molecules in the flow to the equilibrium value of their pervaded volume is represented by the square root of the determinant of the conformation dyadic. In this model, it can change by action of the velocity gradient.

3.2. *Affinely deforming, finitely extensible molecules (FENE-P)*

The hypothesis of the finitely extensible, non-linearly elastic (FENE) equations are: the molecules follow imposed deformations affinely: $\xi \equiv \zeta \equiv 1$; the maximum extension of the molecules is finite, and their rate of relaxation grows infinitely fast as the average molecular extension approaches its maximum value: $g_0 \equiv -1$, $g_1 \equiv (b-1)/(b - \mathrm{Tr}\,\boldsymbol{M}/3)$, $g_2 \equiv 0$. The parameter b controls the molecular extensibility, and is defined as the ratio of the maximum length square of the polymer molecules to their average length square at equilibrium. The derivative of g_1 with respect to the conformation dyadic is needed to derive the partial derivative entries in the Jacobian matrix needed for Newton's method:

$$\frac{\partial g_1}{\partial M_{ij}} = \frac{1}{3}\frac{b-1}{(b - \mathrm{Tr}\,(\boldsymbol{M}/3))^2}\delta_{ij} \tag{12}$$

The evolution equation of the dimensionless conformation dyadic is

$$\dot{\boldsymbol{M}} \equiv \frac{\partial \boldsymbol{M}}{\partial t} + \boldsymbol{v} \cdot \nabla \boldsymbol{M} = \nabla \boldsymbol{v}^{\mathrm{T}} \cdot \boldsymbol{M} + \boldsymbol{M} \cdot \nabla \boldsymbol{v} - \frac{1}{\lambda}\left(\frac{b-1}{b - \mathrm{Tr}\,(\boldsymbol{M}/3)}\boldsymbol{M} - \boldsymbol{I}\right) \tag{13}$$

and the Helmholtz free energy is

$$a \equiv (3/2)G(b-1)\ln\left[\frac{(b-1)}{(b - \mathrm{Tr}\,(\boldsymbol{M}/3)}\right]$$

The non-linear relaxation term in the FENE-P equation puts a limit on the maximum extension achievable by the molecules, and is a significant improvement over its linear counterpart, Eq. (11). The FENE-P relaxation function predicts that in a two-dimensional flow the polymer molecules contract in the neutral direction of the flow [9]. Another variant of the FENE equations, the FENE-CR [31], does not have this property because in the FENE-CR, $g_0 + g_1 = 0$.

3.3. Partially retracting semirigid molecules

The hypotheses of the model are: (1) the molecules follow imposed rotations affinely: $\zeta \equiv 1$; (2) the molecules partially retract instantaneously if a sudden stretch is imposed along their axis, and the extent of the retraction is independent of the stretch of the molecules: $\xi = \text{constant} < 1$; (3) the rate of relaxation of the molecules is a linear function of the distance of the dimensionless conformation tensor $\boldsymbol{M}$ from its equilibrium value $\boldsymbol{I}$: $g_0 \equiv -1$, $g_1 \equiv 1$, $g_2 \equiv 0$. In this case, the evolution equation of the dimensionless conformation dyadic is

$$\dot{\boldsymbol{M}} \equiv \frac{\partial \boldsymbol{M}}{\partial t} + \boldsymbol{v} \cdot \nabla \boldsymbol{M} = 2\xi(\boldsymbol{M})\frac{\boldsymbol{D} : \boldsymbol{M}}{\boldsymbol{I} : \boldsymbol{M}}\boldsymbol{M} + \left(\boldsymbol{M} \cdot \boldsymbol{D} + \boldsymbol{D} \cdot \boldsymbol{M} - 2\frac{\boldsymbol{D} : \boldsymbol{M}}{\boldsymbol{I} : \boldsymbol{M}}\boldsymbol{M}\right) + \boldsymbol{M} \cdot \boldsymbol{W} + \boldsymbol{W}^{\mathrm{T}} \cdot \boldsymbol{M} - \frac{1}{\lambda}(\boldsymbol{M} - \boldsymbol{I}) \tag{14}$$

and the Helmholtz free energy is $a \equiv (G/2)(\mathrm{Tr}\,\boldsymbol{M} - \ln\det \boldsymbol{M})$.

This model was introduced by Larson [32,33] and by Marrucci and Grizzuti [34] to describe the behavior of entangled polymer segments that do not stretch along their backbone but orient collectively by following the imposed rotation [35]. Larson's model captures some of the salient features of the reptation model, and like the reptation model describes reasonably well the near-linear behavior of entangled polymer solutions and melts in shear flow [36].

The partially retracting segment model describes well the behavior of rod-like polymer molecules that are almost or completely rigid [35]; this is how the model is used here. If the stretching resistance $\xi = 0$, the retraction of the segments is complete and their length is constant; if $\xi = 1$, the molecules stretch with the continuum deformation.

3.4. Boundary conditions on transport equations

Boundary conditions are needed on the momentum and conformation transport equations. The momentum boundary conditions are:

(1) *No-slip and no-penetration*: At solid, impermeable boundaries, the velocity of the liquid equals that of the solid, $\boldsymbol{v} = \boldsymbol{v}_w$.

(2) *Force balance at free surfaces*: The tangential traction vanishes at a free surface because the shear stress exerted by the gas on the liquid is negligible, $\boldsymbol{tn}:\boldsymbol{T}=0$; the normal traction inside the liquid must balance the sum of the pressure in the gas p_a and the capillary pressure induced by the curvature of the surface, $\boldsymbol{nn}:\boldsymbol{T}=-p_a+\varsigma\nabla_{\mathrm{II}}\cdot\boldsymbol{n}$, where ς is the surface tension of the liquid, and $\nabla_{\mathrm{II}}\equiv(\boldsymbol{I}-\boldsymbol{nn})\cdot\nabla$ is the surface gradient; in a two-dimensional flow, the normal stress balance can also be written as $\boldsymbol{nn}:\boldsymbol{T}=-p_a+\varsigma\boldsymbol{n}\cdot\mathrm{d}\boldsymbol{t}/\mathrm{d}s$, where $\boldsymbol{t}$ is the tangent to the free surface, and s is arclength along the free surface—in vector form, $\boldsymbol{n}\cdot\boldsymbol{T}=-p_a\boldsymbol{n}+\varsigma\mathrm{d}\boldsymbol{t}/\mathrm{d}s$.

(3) *Inflow and outflow conditions*: A velocity profile is prescribed at the open boundary, $\boldsymbol{v}=\boldsymbol{v}_0(\boldsymbol{x})$, or a pressure datum is specified through the integral of the traction $\boldsymbol{n}\cdot\boldsymbol{t}$ at the open boundary, or the fully developed flow condition is imposed, $\boldsymbol{n}\cdot\nabla\boldsymbol{v}=\boldsymbol{0}$, also through the boundary integral of the traction. The former two boundary conditions are normally used at inflows, the latter at outflows. Of course, the solution of the problem must prove insensitive to the location of the open boundaries.

(4) *Symmetry*: The liquid cannot cross a symmetry line or surface, $\boldsymbol{n}\cdot\boldsymbol{v}=0$, and the shear stress vanishes there, $\boldsymbol{tn}:\boldsymbol{T}=0$.

The transport equation of conformation Eq. (7) is hyperbolic and its characteristics in a steady flow are the streamlines; therefore boundary conditions are needed only on inflow boundaries. Because Eq. (7) is a tensor equation, tensor boundary conditions must be imposed. The only exception is the flow of polymer solutions whose stress is purely elastic ($\boldsymbol{\tau}=0$), where only the normal and tangential components of the conformation dyadic must be specified at the inflow boundaries [37,38].

The components of the conformation dyadic at an inflow boundary are not known in general. Commonly, in viscoelastic flow computations the inflow boundaries are placed in regions of fully developed, parallel, and rectilinear flow, where the profile of conformation is known analytically or it can be computed in advance. Given a fixed inflow velocity profile, the inflow conformation profile depends on the choice of constitutive functions in the transport equations; therefore the common procedure of imposing inflow boundary conditions on conformation is not amenable to generalization.

If the flow at the inflow boundary is fully developed, the conformation of the polymer there does not change along the streamlines, $\boldsymbol{v}\cdot\nabla\boldsymbol{M}=0$, and the algebraic equation

$$\begin{aligned}0=&-2\xi\frac{\boldsymbol{D}:\boldsymbol{M}}{\boldsymbol{I}:\boldsymbol{M}}\boldsymbol{M}-\zeta\left(\boldsymbol{M}\cdot\boldsymbol{D}+\boldsymbol{D}\cdot\boldsymbol{M}-2\frac{\boldsymbol{D}:\boldsymbol{M}}{\boldsymbol{I}:\boldsymbol{M}}\boldsymbol{M}\right)\\&-\boldsymbol{M}\cdot\boldsymbol{W}-\boldsymbol{W}^{\mathrm{T}}\cdot\boldsymbol{M}+\frac{1}{\lambda}(g_0\boldsymbol{I}+g_1\boldsymbol{M}+g_2\boldsymbol{M}^2)\end{aligned}\qquad(15)$$

holds at the boundary. Eq. (15) is independent of constitutive assumptions and is enforced strongly as tensor boundary condition at the inflow portions of open boundaries. Of course, an equivalent equation applies if elastic stress rather than conformation is used as independent variable.

4. Modified transport equations

Three modifications to the transport equations are made before the equation set is cast in the weighted residual form.

4.1. *Velocity gradient interpolation*

As suggested by Szady et al. [5], an additional variable $\boldsymbol{L}$ is introduced to represent the velocity gradient with a continuous interpolation:

$$0 = \boldsymbol{L} - \nabla \boldsymbol{v} \tag{16}$$

The variable $\boldsymbol{L}$ is called *interpolated velocity gradient* in the following to distinguish it from the *raw velocity gradient* $\nabla \boldsymbol{v}$. The rate of strain dyadic $\boldsymbol{D}$ and the vorticity dyadic $\boldsymbol{W}$ in the transport equation of conformation are computed using the interpolated velocity gradient $\boldsymbol{L}$,

$$\boldsymbol{D} \equiv \tfrac{1}{2}(\boldsymbol{L} + \boldsymbol{L}^{\mathrm{T}}), \qquad \boldsymbol{W} \equiv \tfrac{1}{2}(\boldsymbol{L} - \boldsymbol{L}^{\mathrm{T}}) \tag{17}$$

4.2. *Traceless interpolated velocity gradient*

In incompressible flows the trace of the velocity gradient vanishes, $\nabla \cdot \boldsymbol{v} = \mathrm{Tr}\, \boldsymbol{L} = 0$. The approximate velocity field computed with the weighted residual/finite element method is not exactly divergence-free, and the approximate value of the interpolated velocity gradient is not exactly traceless. If the weighting functions used in Eqs. (5) and (16) are different, the trace of the interpolated velocity gradient becomes dangerously large in flow regions where the velocity changes abruptly. $\mathrm{Tr}\, \boldsymbol{L} \approx 0.1\dot{\gamma}^{\max}$ is common on coarse meshes, and $\mathrm{Tr}\, \boldsymbol{L} \approx 0.01\dot{\gamma}^{\max}$ is typical on more refined meshes (see [9] for details). Here $\dot{\gamma}^{\max}$ is the maximum of the positive eigenvalue of the rate of strain dyadic in the whole flow field.

The rate of change along the streamlines of the determinant of the conformation dyadic is directly related to $\mathrm{Tr}\, \boldsymbol{L}$. The formula of the derivative of the determinant of a dyadic ([39], p. 26) and Eq. (7) lead to the equation of change of the determinant of the conformation tensor,

$$\frac{\mathrm{D}}{\mathrm{D}t} \ln \det \boldsymbol{M} = 6(\xi - \zeta)\frac{\boldsymbol{D} : \boldsymbol{M}}{\boldsymbol{I} : \boldsymbol{M}} + 2\,\mathrm{Tr}\, \boldsymbol{D} - \frac{1}{\lambda}(g_0\, \mathrm{Tr}\, \boldsymbol{M}^{-1} + 3g_1 + g_2\, \mathrm{Tr}\, \boldsymbol{M}) \tag{18}$$

The determinant of the conformation dyadic must be positive because $\boldsymbol{M}$ is positive definite. If $\mathrm{Tr}\, \boldsymbol{L}$ is computed inaccurately, $\det \boldsymbol{M}$ could change sign, leading to meaningless computational results. The trace of $\boldsymbol{L}$ can be computed accurately with the equation

$$0 = \boldsymbol{L} - \nabla \boldsymbol{v} + \frac{1}{\mathrm{Tr}\, \boldsymbol{I}}(\nabla \cdot \boldsymbol{v})\boldsymbol{I} \tag{19}$$

in place of Eq. (16). Eq. (19) guarantees that $\mathrm{Tr}\, \boldsymbol{L} = 0$ regardless of the value of $\nabla \cdot \boldsymbol{v}$.

4.3. *Discrete adaptive viscous stress split*

Guénette and Fortin [4] wrote the inertialess momentum equation as

$$\nabla \cdot (-p\boldsymbol{I} + \boldsymbol{\sigma}) + \nabla \cdot \eta_a(\nabla \boldsymbol{v} + \nabla \boldsymbol{v}^{\mathrm{T}} - \boldsymbol{L} - \boldsymbol{L}^{\mathrm{T}}) = 0 \tag{20}$$

where η_a is a numerical parameter, and showed that the last term in Eq. (20) stabilized the computational method. The assumption of Guénette and Fortin can also be explained by noting that either the raw, or the interpolated velocity gradient, or a combination of both can be used to compute the viscous stress in Eq. (9), and that the relation

$$\boldsymbol{\tau} = \mu(\boldsymbol{L} + \boldsymbol{L}^{\mathrm{T}}) + \eta_a(\nabla \boldsymbol{v} + \nabla \boldsymbol{v}^{\mathrm{T}} - \boldsymbol{L} - \boldsymbol{L}^{\mathrm{T}}) \tag{21}$$

together with the momentum transport equation leads to Eq. (20).

There is no difference between the interpretation of Eq. (20) given by Guénette and Fortin and that offered here with Eq. (21) if velocity boundary conditions are imposed on the momentum equation on all boundaries, as is usually done in confined viscoelastic flows. However, the two interpretations lead to different ways of handling the traction boundary conditions used in free surface flows.

Interpreting the term $\eta_a(\nabla \boldsymbol{v} + \nabla \boldsymbol{v}^{\mathrm{T}} - \boldsymbol{L} - \boldsymbol{L}^{\mathrm{T}})$ as a stabilizing element in the momentum equation compels that its boundary integral be accounted for at a free surface; conversely, defining the viscous stress with Eq. (21) yields no contribution other than those of the ambient and capillary pressures to the boundary integral of the traction at a free surface. The latter approach is taken here. Computations were made with a constant value of η_a. Changing the value of η_a had little or no effect on the solution of the flows, provided that η_a was comparable to μ.

5. Weighted residual equations

Multiplying Eqs. (1), (5)–(7), and (19), by weighting functions $\psi_{\boldsymbol{x}}$, ψ_c, $\psi_{\boldsymbol{m}}$, $\psi_{\boldsymbol{M}}$, and $\psi_{\boldsymbol{L}}$, integrating over the (unknown) physical domain Ω (bounded by Γ), applying the Gauss–Green–Ostrogradskii theorem to the mesh generation equation and to the momentum equation, and mapping the integrals onto the (known) computational domain Ω_0 (bounded by Γ_0) yields the weighted residual equations:

$$\boldsymbol{r}^{\boldsymbol{x},\alpha} = \int_{\Gamma_0} \boldsymbol{n} \cdot \psi_{\boldsymbol{x}}^{\alpha} \tilde{\boldsymbol{D}} \cdot \nabla \boldsymbol{\xi}\, \ell \,\mathrm{d}\Gamma_0 - \int_{\Omega_0} \nabla \psi_{\boldsymbol{x}}^{\alpha} \cdot \tilde{\boldsymbol{D}} \cdot \nabla \boldsymbol{\xi}\, f \,\mathrm{d}\Omega_0 \tag{22}$$

$$r^{c,\alpha} = \int_{\Omega_0} \psi_c^{\alpha} \nabla \cdot \boldsymbol{v}\, f \,\mathrm{d}\Omega_0 \tag{23}$$

$$\boldsymbol{r}^{\boldsymbol{m},\alpha} = \int_{\Omega_0} \psi_{\boldsymbol{m}}^{\alpha} (\rho \boldsymbol{v} \cdot \nabla \boldsymbol{v} - \nabla \Theta)\, f \,\mathrm{d}\Omega_0 + \int_{\Omega_0} \nabla \psi_{\boldsymbol{m}}^{\alpha} \cdot \boldsymbol{T} f \,\mathrm{d}\Omega_0 - \int_{\Gamma_0} \boldsymbol{n} \cdot \psi_{\boldsymbol{m}}^{\alpha} \boldsymbol{T} \ell \,\mathrm{d}\Gamma_0 \tag{24}$$

$$\boldsymbol{R}^{\boldsymbol{L},\alpha} = \int_{\Omega_0} \psi_{\boldsymbol{L}}^{\alpha} \left(\boldsymbol{L} - \nabla \boldsymbol{v} + \frac{1}{\mathrm{Tr}\, \boldsymbol{I}} (\nabla \cdot \boldsymbol{v}) \boldsymbol{I} \right) f \,\mathrm{d}\Omega_0 \tag{25}$$

$$\begin{aligned} \boldsymbol{R}^{\boldsymbol{M},\alpha} = \int_{\Omega_0} \psi_{\boldsymbol{M}}^{\alpha} \Bigg(& \boldsymbol{v} \cdot \nabla \boldsymbol{M} - 2\xi \frac{\boldsymbol{D} : \boldsymbol{M}}{\boldsymbol{I} : \boldsymbol{M}} \boldsymbol{M} - \zeta \left(\boldsymbol{M} \cdot \boldsymbol{D} + \boldsymbol{D} \cdot \boldsymbol{M} - 2 \frac{\boldsymbol{D} : \boldsymbol{M}}{\boldsymbol{I} : \boldsymbol{M}} \boldsymbol{M} \right) \\ & - \boldsymbol{M} \cdot \boldsymbol{W} - \boldsymbol{W}^{\mathrm{T}} \cdot \boldsymbol{M} + \frac{1}{\lambda} (g_0 \boldsymbol{I} + g_1 \boldsymbol{M} + g_2 \boldsymbol{M}^2) \Bigg) f \,\mathrm{d}\Omega_0 \end{aligned} \tag{26}$$

$\boldsymbol{n}$ is the outward pointing normal to the boundary Γ;

$$\ell \equiv \frac{\mathrm{d}\Gamma}{\mathrm{d}\Gamma_0} = \det \boldsymbol{F} \sqrt{\boldsymbol{n}^0 \cdot \boldsymbol{K}^{\mathrm{T}} \cdot \boldsymbol{K} \cdot \boldsymbol{n}^0} \tag{27}$$

is the ratio of the magnitudes of infinitesimal elements of boundary of the physical and computational domain ; $\boldsymbol{n}^0$ is the outward pointing unit normal to the computational domain, $\boldsymbol{n} = (f/\ell)\boldsymbol{K} \cdot \boldsymbol{n}^0$;

$$f \equiv \frac{\mathrm{d}\Omega}{\mathrm{d}\Omega_0} = \det \boldsymbol{F} \tag{28}$$

is the Jacobian of the mapping, and represents the ratio of magnitudes of infinitesimal elements of the physical and computational domains;

$$\boldsymbol{F} \equiv \triangleleft \boldsymbol{x} \equiv \frac{\partial \boldsymbol{x}}{\partial \boldsymbol{\xi}} \equiv \triangleleft \varphi_{\boldsymbol{x}}^{\beta} \boldsymbol{x}^{\beta}, \qquad F_{ij} \equiv \frac{\partial x_j}{\partial \xi_i} \equiv \triangleleft_i \, x_j \equiv x_j^{\beta} \frac{\partial \varphi_{\boldsymbol{x}}^{\beta}}{\partial \xi_i} \tag{29}$$

is the mapping deformation gradient; $\triangleleft$ denotes the gradient in the computational domain;[1] and the indices i, j denote direction in physical space.

The gradient in physical space ∇ is related to the gradient in computational space $\triangleleft$ by the relation

$$\nabla \mathcal{G} = \boldsymbol{K} \cdot \triangleleft \mathcal{G}, \qquad \nabla_i \mathcal{G} \equiv \frac{\partial \mathcal{G}}{\partial x_i} = K_{ij} \frac{\partial \mathcal{G}}{\partial \xi_j} \equiv K_{ij} \triangleleft_j \mathcal{G} \tag{30}$$

where $\mathcal{G}$ can be any physical quantity—scalar, vector, dyadic, or tensor component—and $\boldsymbol{K}$ is the inverse mapping deformation gradient,

$$\boldsymbol{K} \equiv \nabla \boldsymbol{\xi} \equiv \frac{\partial \boldsymbol{\xi}}{\partial \boldsymbol{x}} = \boldsymbol{F}^{-1}, \qquad K_{ij} \equiv \frac{\partial \xi_j}{\partial x_i} \tag{31}$$

Each independent variable is approximated with a linear combination of finite number of basis functions $\boldsymbol{x} \equiv \boldsymbol{x}^{\beta} \varphi_{\boldsymbol{x}}^{\beta}$, $p \equiv p^{\beta} \varphi_p^{\beta}$, $\boldsymbol{v} \equiv \boldsymbol{v}^{\beta} \varphi_{\boldsymbol{v}}^{\beta}$, $\boldsymbol{L} \equiv \boldsymbol{L}^{\beta} \varphi_{\boldsymbol{L}}^{\beta}$, and $\boldsymbol{M} \equiv \boldsymbol{M}^{\beta} \varphi_{\boldsymbol{M}}^{\beta}$; to lighten the notation, the same symbols $\boldsymbol{x}$, p, $\boldsymbol{v}$, $\boldsymbol{L}$, and $\boldsymbol{M}$ are used to represent the approximate value of the independent variables, as in Eqs. (22)–(26), and their exact value, as in Eqs. (1), (5)–(7), and (19). The context makes clear whether the exact or approximate value is referenced.

The basis functions used to represent the independent variables are: Lagrangian biquadratic for position ($\varphi_{\boldsymbol{x}}$) and velocity ($\varphi_{\boldsymbol{v}}$), linear discontinuous for pressure (φ_p), and Lagrangian bilinear for interpolated velocity gradient ($\varphi_{\boldsymbol{L}}$) and conformation ($\varphi_{\boldsymbol{M}}$). Galerkin weighting functions are used in the residual equations of mesh generation ($\psi_{\boldsymbol{x}} \equiv \varphi_{\boldsymbol{x}}$), continuity ($\psi_c \equiv \varphi_p$), momentum ($\psi_{\boldsymbol{m}} \equiv \varphi_{\boldsymbol{v}}$), and velocity gradient interpolation ($\psi_{\boldsymbol{L}} \equiv \varphi_{\boldsymbol{L}}$), whereas streamline upwind Petrov–Galerkin weighting functions are used in the conformation transport equation ($\psi_{\boldsymbol{M}} \equiv \varphi_{\boldsymbol{M}} + h^u \boldsymbol{v} \cdot \nabla \varphi_{\boldsymbol{M}}$), where h^u is the upwind parameter—the characteristic size of the smallest element in the mesh.

6. Newton's method with analytical Jacobian

The system of non-linear algebraic equations Eqs. (22)–(26) is solved with Newton's method with analytical Jacobian. The tolerance on the 2-norm of the residual and Newton update was set to 10^{-6}. The linear system was solved with a frontal solver based on the algorithm of Duff et al. [9,43].

The formulae of the analytical derivatives of Eqs. (22)–(26) and their boundary conditions with respect to the basis function coefficients $\boldsymbol{x}^{\beta}$, p^{β}, $\boldsymbol{v}^{\beta}$, $\boldsymbol{L}^{\beta}$, and $\boldsymbol{M}^{\beta}$ must be evaluated to compute the entries of the Jacobian matrix. Table 1 shows the incidence matrices of Eqs. (22)–(26) and their boundary conditions. If each physical component of the residual equations and each component of the unknown variables is considered a separate scalar, as is commonly done, the equation set has 13 equations in 13 unknowns in a two-dimensional flow, and 22 equations in as many unknowns in a three-dimensional flow, which leads to approximately 180 and 520 non-zero derivatives in a two- and three-dimensional

---

[1] The symbol $\triangleleft$ was originally used by Hamilton [40,41] to represent the gradient of a quaternion [42].

Table 1
Incidence matrices of the residual equations and their boundary conditions

Equation	Unknown									
	Analytical Jacobian residual equations					Analytical Jacobian boundary conditions				
	$\boldsymbol{x}$	p	$\boldsymbol{v}$	$\boldsymbol{L}$	$\boldsymbol{M}$	$\boldsymbol{x}$	p	$\boldsymbol{v}$	$\boldsymbol{L}$	$\boldsymbol{M}$
Mesh generation	✓					✓		✓		
Continuity	✓		✓							
Momentum transport	✓	✓	✓	✓	✓	✓	✓	✓	✓	✓
Velocity gradient interpolation	✓		✓	✓						
Conformation transport	✓		✓	✓	✓				✓	✓

A checkmark (✓) in a matrix entry indicates that the equation in the row of the entry depends on the variable in the column of the entry.

flow respectively—including entries due to boundary conditions. On the other hand, only 24 derivatives (4 vectors, 7 second-rank tensors, 8 third-rank tensors, and 5 fourth-rank tensor derivatives) are needed if the equations and unknowns are kept in their vector or dyadic form, regardless of whether a two- or three-dimensional flow is computed. The latter approach is followed here. The formulae of the derivatives of the residual equations with respect to the basis function coefficients are reported in Appendix A. The area and line integrals in the formulae of the weighted residuals and analytical Jacobian are evaluated by 9- and 3-point Gaussian integration, respectively.

The residual vector and Jacobian matrix are assembled by mapping the scalar, vector, and tensor residuals and derivatives into an algebraic vector and matrix, respectively. Because the residuals of the transport equation of conformation $\boldsymbol{R}^{\boldsymbol{M},\alpha}$ are symmetric, the residuals $R_{ij}^{\boldsymbol{M},\alpha}$ are assembled only for $i \leq j$. Because $\boldsymbol{M}$ is symmetric, only M_{ij}, $i \leq j$ are necessary as independent variables; the derivatives of the residual equations with respect to the basis function coefficients of the off-diagonal components of the conformation dyadic are:

$$J(\mathsf{id}(r_k^{\boldsymbol{m},\alpha}), \mathsf{jd}(M_{ij}^{\gamma})) = \frac{\partial r_k^{\boldsymbol{m},\alpha}}{\partial M_{ij}^{\gamma}} + \frac{\partial r_k^{\boldsymbol{m},\alpha}}{\partial M_{ji}^{\gamma}},$$

$$\alpha = 1, \ldots, N^{\boldsymbol{m}}; \quad \gamma = 1, \ldots, N^{\boldsymbol{M}}, \quad k, i, j = 1, \ldots, n^{\text{dir}}; \quad j > i \tag{32}$$

where id and jd are the mapping pointers (see [9] for details).

6.1. Initialization of Newton's method and parameter continuation strategy

An initial guess for Newton's method was generated as follows:

(1) The initial shape of the free surfaces was approximated by a straight line or by a combination of straight lines and arcs of circles. The equations of the inertialess flow of a Newtonian liquid were solved by treating the free surfaces as perfectly slippery boundaries.
(2) The solution of this linear problem was used as the initial guess to solve the non-linear equations describing the free surface flow of a Newtonian liquid.
(3) The interpolated velocity gradient $\boldsymbol{L}$ was then computed by fixing velocity, pressure, and location of the free surfaces.

(4) The polymer conformation dyadic $\boldsymbol{M}$ was then computed by fixing velocity, pressure, location of the free surfaces, and interpolated velocity gradient at a low value of the Weissenberg number, typically $Ws = 0.01$, using the initial guess $\boldsymbol{M} = \boldsymbol{I}$ for the polymer conformation dyadic ($\boldsymbol{M} = \boldsymbol{I} + 2Ws\boldsymbol{D}$ is a more accurate initial guess; however the simpler initial guess $\boldsymbol{M} = \boldsymbol{I}$ was always inside the radius of convergence of Newton's method in the cases examined).

The values of velocity, pressure, location of the free surfaces, interpolated velocity gradient, and polymer conformation so computed are those that occur in the flow of an infinitely dilute solution of polymer with a finite relaxation time and infinitely small elastic modulus, where there is no coupling between the momentum equation and the polymer conformation dyadic. The solution of this last problem provided a robust initial guess with which to compute the free surface flow of a polymer solution.

Solutions at different values of parameters were then generated with first-order arclength continuation [22]. The size of the continuation step was doubled automatically if Newton's method converged in three iterations or less, and was quartered if Newton's method converged in more than six iterations, if it failed to converge, if the mesh folded, or if the conformation dyadic lost positive definiteness anywhere in the flow domain.

7. Indicators of local molecular and flow behavior

7.1. *Molecular stretch and orientation*

The solutions of equations of viscoelastic flow are often reported by showing the distributions of Cartesian components of the elastic stress dyadic. These distributions are difficult to interpret because the relationship between the Cartesian components of the stress dyadic and the microstructural state of the polymer is not immediately apparent.

The invariants of the conformation dyadic are immediately accessible measures of the microstructural state of the polymer in various regions of the flow. They are excellent means of displaying the results of viscoelastic flow calculations.

The orthonormal eigenvectors $\boldsymbol{m}_i$ of the conformation dyadic represent the three mutually orthogonal directions along which molecules are oriented and stretched, or contracted—the principal directions of the second moment of the distribution of stretch and orientation. The eigenvalues m_i represent the square of the principal stretch ratios of flowing ensembles of polymer segments, i.e. the average length square of polymer segments along the principal directions of stretch divided by the length square of the segments at equilibrium. The square root of the determinant of $\boldsymbol{M}$ is the ratio of the volume pervaded by the flowing molecules to the volume pervaded by the molecules at equilibrium. The eigenvalues of $\boldsymbol{M}$ are always real and positive because $\boldsymbol{M}$ is symmetric and positive definite. Hereafter, the convention is used $m_1 \leq m_2 \leq m_3$ to order the eigenvalues of conformation.

7.2. *Molecular extension and shear rate*

The classical definitions of shear and extension rates ([44], p.155, p. 162) are based on the Cartesian components of the velocity gradient referred to conveniently chosen spatially uniform orthonormal basis vectors; they cannot be applied to flow where the velocity gradient is not homogeneous.

The invariants of the rate of strain cannot serve as indicators of the type of flow because they do not carry any information on whether polymer molecules are being strained persistently along the same axes—the essence of extensional flow—or are rotating with respect to the principal axes of the rate of strain, so that each molecule is alternatively elongated and contracted by the rate of strain—the essence of shear flow. The vorticity depends on the choice of frame of reference, and by itself cannot provide indications on the local type of flow, although relative rotation rates defined as the difference between the vorticity and other rates of rotation have been used to index the flow type [45,46]. The invariants of the conformation dyadic (or elastic stress) cannot be used to index the local flow type because they contain information on the whole upstream history of deformation and because they are affected by the intensity of the straining as well as the type of deformation.

The chief difference between extensional and shear flows is that in extension polymer molecules are being stretched along the preferred direction(s) of stretch and orientation, and are being contracted along the direction(s) where they are already contracted and least likely to be oriented, whereas in a shear flow the principal directions of stretching do not coincide with the principal directions of molecular stretch and orientation. This important physical difference suggests defining a mean ensemble molecular extension rate as the rate of strain along the eigenvector $\boldsymbol{m}_3$ associated with the largest eigenvalue of $\boldsymbol{M}$:

$$\dot{\varepsilon}_{\boldsymbol{M}} \equiv \boldsymbol{m}_3\boldsymbol{m}_3 : \boldsymbol{D} \tag{33}$$

The molecular extension rate $\dot{\varepsilon}_{\boldsymbol{M}}$ is independent of choice of frame of reference. Where $\dot{\varepsilon}_{\boldsymbol{M}} > 0$, polymer segments are being stretched along their direction of preferred stretch and orientation and the flow is working against the molecular relaxation processes; where $\dot{\varepsilon}_{\boldsymbol{M}} < 0$, the flow and the relaxation processes work together towards restoring the equilibrium length of the polymer segments, i.e. the liquid is recoiling.

The molecular shear rate is defined as the rate of strain along $\boldsymbol{m}_1$ of molecules aligned with $\boldsymbol{m}_3$:

$$\dot{\gamma}_{\boldsymbol{M}} \equiv |\boldsymbol{m}_1\boldsymbol{m}_3 : \boldsymbol{D}| \tag{34}$$

because $\boldsymbol{D}$ is symmetric, $\dot{\gamma}_{\boldsymbol{M}}$ is also the rate of strain along $\boldsymbol{m}_3$ of molecules aligned with $\boldsymbol{m}_1$. The absolute value appears in Eq. (34) because $\boldsymbol{m}_1$, $-\boldsymbol{m}_1$, $\boldsymbol{m}_3$, and $-\boldsymbol{m}_3$ are unit eigenvectors of the conformation dyadic, but the definition of $\dot{\gamma}_{\boldsymbol{M}}$ must be independent of the sign of $\boldsymbol{m}_1$ and $\boldsymbol{m}_3$. A large $\dot{\gamma}_{\boldsymbol{M}}$ indicates that the rate of strain is deforming molecules aligned along one of the principal directions of the conformation tensor in a direction orthogonal to their orientation; it is stretching or contracting along their axes the molecules that are aligned at 45° with respect to the principal directions of the conformation tensor.

In two-dimensional, incompressible flows there is only one independent molecular extension rate and one independent molecular shear rate, whereas in three-dimensional flows there are two independent molecular extension rates and three independent molecular shear rates; they coincide, respectively with the diagonal and off-diagonal entries of the matrix of components of $\boldsymbol{D}$ in a curvilinear orthogonal coordinate system whose basis coincides locally with the eigenvectors of $\boldsymbol{M}$ everywhere in the flow.

The molecular extension and shear rates can be used to define extensional and shear flow indices:

$$e \equiv \frac{\dot{\varepsilon}^2_{1,\boldsymbol{M}} + \dot{\varepsilon}^2_{2,\boldsymbol{M}} + \dot{\varepsilon}^2_{3,\boldsymbol{M}}}{-2II_{\boldsymbol{D}}}, \qquad s \equiv \frac{\dot{\gamma}^2_{12,\boldsymbol{M}} + \dot{\gamma}^2_{23,\boldsymbol{M}} + \dot{\gamma}^2_{31,\boldsymbol{M}}}{-II_{\boldsymbol{D}}}, \qquad e + s = 1 \tag{35}$$

In two-dimensional flows, Eq. (35) simplifies to

$$e \equiv \frac{\dot{\varepsilon}^2_{\boldsymbol{M}}}{d^2}, \qquad s \equiv \frac{\dot{\gamma}^2_{\boldsymbol{M}}}{d^2} \tag{36}$$

where d is the positive eigenvalue of $\boldsymbol{D}$.

The extension and shear flow indicators defined by Eq. (35) are always well-defined because if $II_{\boldsymbol{D}}$ vanishes, the whole rate of strain dyadic must vanish too.

When applied to homogeneous extensional flow, the flow indicators signal that the flow is purely extensional ($e = 1,\ \ s = 0$). However, in simple shear flow their values depend on both the choice of model and the Weissenberg number because these determine the orientation of the eigenvectors of the conformation dyadic. At low Weissenberg number, e approaches unity whereas s nearly vanishes because $\boldsymbol{M} \approx \boldsymbol{I} + 2\,Ws\,\boldsymbol{D}$ and thus the eigenvectors of $\boldsymbol{M}$ and $\boldsymbol{D}$ coincide. At high Weissenberg number the eigenvectors of $\boldsymbol{M}$ tend to align with the velocity ($\boldsymbol{m}_3$) and the gradient ($\boldsymbol{m}_1$); thus $e \to 0$ and $s \to 1$.

Although the flow indicators, Eq. (35), do not classify shear flows according to the traditional definitions (i.e. independent of model and Weissenberg number), they give more faithful information on the coupling of flow and polymer behavior than the traditional definitions. The linearized version of Eq. (7)at low Weissenberg number is

$$Ws(-\boldsymbol{v}\cdot\nabla\boldsymbol{M} + \nabla\boldsymbol{v}^{\mathrm{T}}\cdot\boldsymbol{M} + \boldsymbol{M}\cdot\nabla\boldsymbol{v}) - (\boldsymbol{M} - \boldsymbol{I}) = 0$$

setting $\boldsymbol{M} \equiv \boldsymbol{I} + \epsilon\hat{\boldsymbol{M}}$, where ϵ is a small parameter, yields

$$\underbrace{2Ws\boldsymbol{D} - \epsilon\hat{\boldsymbol{M}}}_{\text{first order}} + \underbrace{\epsilon Ws(-\boldsymbol{v}\cdot\nabla\hat{\boldsymbol{M}} + \boldsymbol{D}\cdot\hat{\boldsymbol{M}} + \hat{\boldsymbol{M}}\cdot\boldsymbol{D} + \boldsymbol{W}^{\mathrm{T}}\cdot\hat{\boldsymbol{M}} + \hat{\boldsymbol{M}}\cdot\boldsymbol{W})}_{\text{second order}} = 0 \tag{37}$$

i.e. the vorticity enters the equation of change of $\boldsymbol{M}$ at second order. In physical terms, at low Ws the polymer is nearly undistorted and thus it does not feel the vorticity and behaves as if it were in extensional flow.

8. Comparison with published studies on confined viscoelastic flows and Newtonian free surface flows

The equations of the theory were programmed in a Fortran 90 computational code (see [9] for details). The correctness of the computer code was checked by comparing the analytical Jacobian to a centered-difference numerical Jacobian; by monitoring the quadratic convergence 2-norm of the residual vector in the terminal Newton iterations; by compiling the code on seven different computer systems and solving the same problem; and by solving a number of problems whose solution could be checked against independently obtained solutions.

Some computations in the early stages of development of the code were made with the numerical Jacobian in place of the analytical Jacobian. The time to compute the numerical Jacobian was large; moreover, loss of quadratic convergence at moderate values of the Weissenberg number was observed when a numerical Jacobian was used (see [9] for details).

8.1. Flow around a cylinder between parallel fixed planes

The flow of a Newtonian liquid and an Oldroyd-B liquid around a cylinder between parallel fixed planes was analyzed, and the drag force on the cylinder was calculated and compared to the analytical solution of Faxén [47], and to the finite element solution of Sun et al. [21].

The flow domain, meshes, and boundary conditions are shown in Figs. 2 and 3. The ratio of cylinder diameter to slit width was set to 1/8, as in [21]. The location of the inflow and outflow boundaries coincides

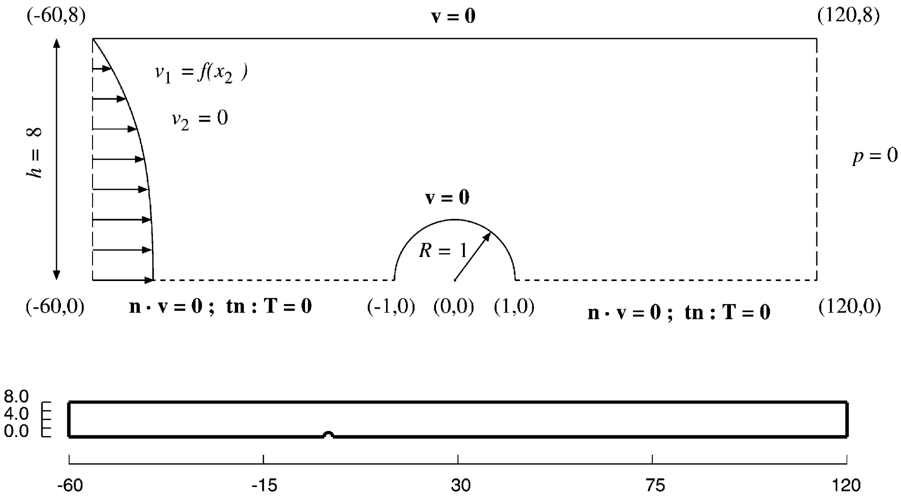

Fig. 2. Flow domain and boundary conditions used to analyze the flow of a Newtonian liquid and an Oldroyd-B liquid around a cylinder. The top drawing is not to scale.

with that chosen by Sun et al., who showed that the flow is insensitive to further displacement of the open boundaries in the range of Weissenberg numbers examined.

The drag force per unit length of the cylinder was computed as

$$f_d \equiv -2 \int_S \boldsymbol{e}_1 \boldsymbol{n} : \boldsymbol{T} \, \mathrm{d}S \tag{38}$$

where S is the surface of the half-cylinder, $\boldsymbol{e}_1$ the horizontal unit vector, and $\boldsymbol{n}$ is the unit normal pointing from the liquid into the cylinder. The integral was computed with 3-point Gaussian quadrature. In the inertialess Newtonian case, the drag force computed on the three different meshes agreed with the values calculated with Faxen's formula and reported by Sun et al. to within 0.05% (see [9] for details).

8.1.1. Imposed flow rate, Oldroyd-B liquid

The flow of an Oldroyd-B liquid was analyzed and the drag force exerted by the liquid on the cylinder was computed as a function of the Weissenberg number $Ws \equiv Q\lambda/hR$. The ratio of solvent viscosity to total viscosity

$$\beta \equiv \frac{\mu}{\mu + \eta_p} = \frac{\mu}{\mu + G\lambda} = 0.59 \tag{39}$$

was used in all calculations, where $\eta_p \equiv G\lambda$ is the polymer contribution and μ is the solvent contribution to the viscosity of the liquid.

The value of the drag force computed on three different meshes with the three different values of adaptive viscosity and the drag force reported by Sun et al. [21] are all in excellent agreement up to $Ws = 2$, as displayed in Fig. 4. At $Ws = 2.2$ the difference between the computed drag and that reported by Sun et al. is approximately 1%.

To ensure that the solutions had converged, the maximum values of the unknowns computed on Mesh1 and Mesh3 were computed. At $Ws = 1$, the maximum values of the velocity components, the pressure,

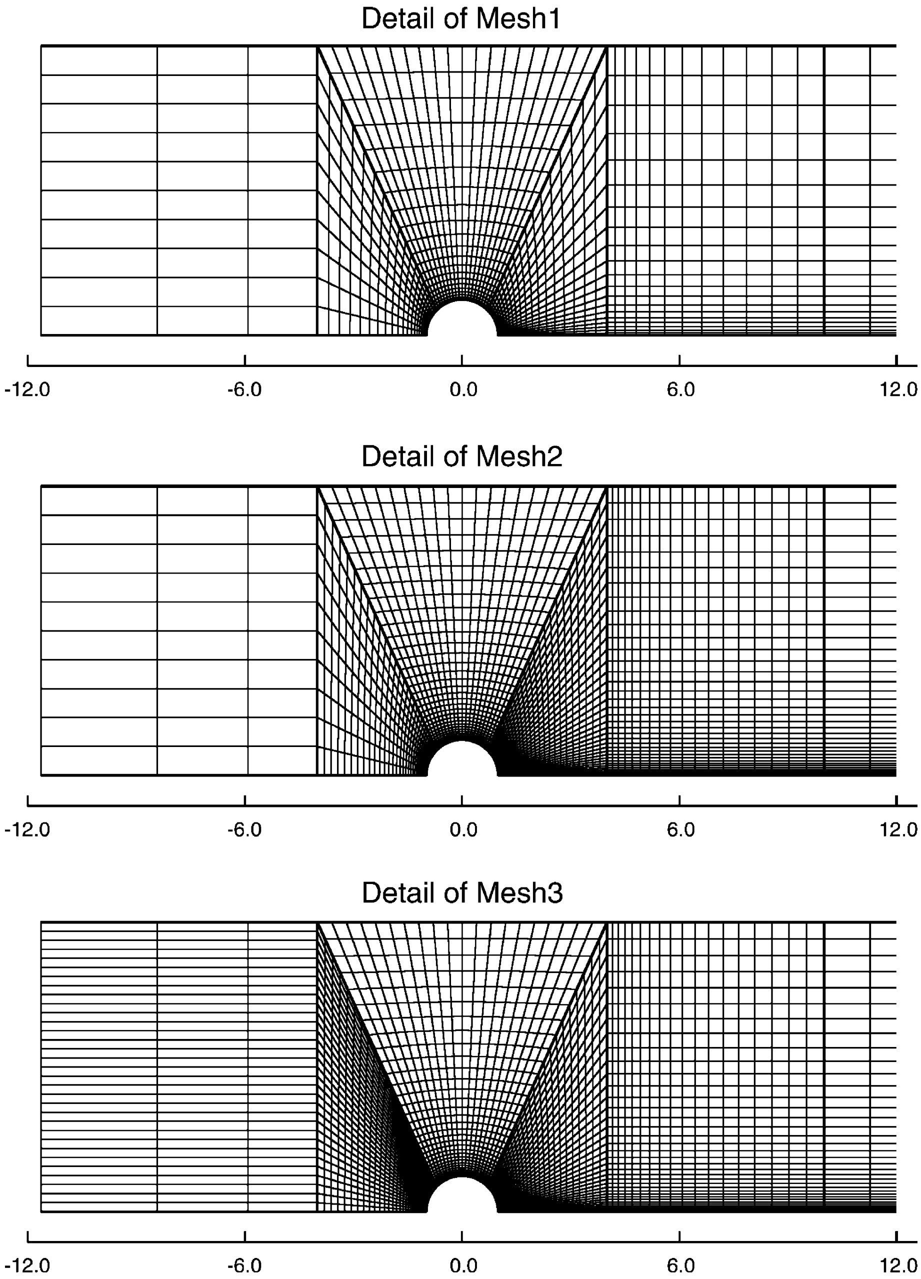

Fig. 3. Detail of the finite element meshes: Mesh1, Mesh2, and Mesh3 used to study flow around a cylinder. Mesh2 has the same refinement of Mesh1 upstream of the cylinder, and the same refinement Mesh3 downstream of the cylinder.

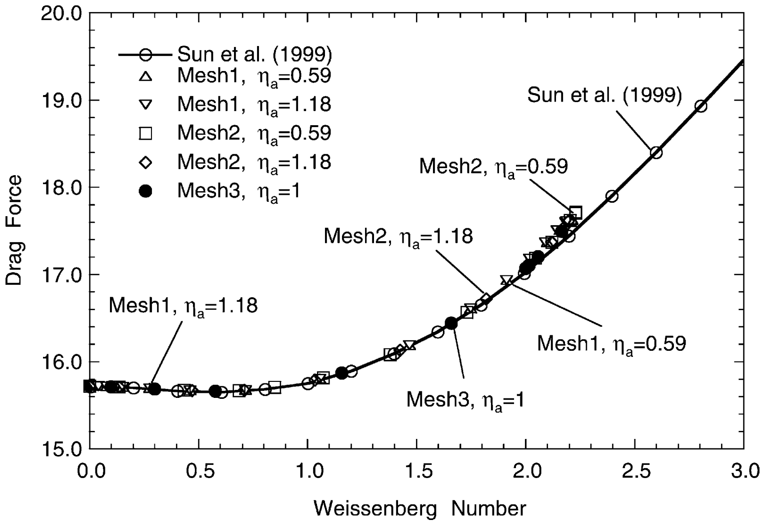

Fig. 4. Drag force f_d exerted by an Oldroyd-B liquid on a stationary cylinder in a channel, as a function of the Weissenberg number. The values are shown of the drag force computed on three different meshes and with different values of the adaptive viscosity η_a. The results of Sun et al. [21] (Fig. 9) are reported for comparison.

and the interpolated velocity gradient components computed on Mesh1 and Mesh3 agreed to within 0.1%, the maximum values of the conformation components agreed to within 0.7%. At $Ws = 2$, the maximum values of the basis function coefficients agreed to within 3%, except for the maximum values of the streamwise normal conformation components, which differed by 7.7%. The maximum and minimum values of velocity, pressure, and elastic stress at $Ws = 2$ reported by Sun et al. ([21], Fig. 11) are compared to those computed on Mesh3 in Table 2. The agreement between the computational results reported here and those reported by Sun et al. is excellent, except for the 54% difference between the maximum values of the streamwise normal elastic stress $\sigma_{11}^{\max}$ in the wake of the cylinder, which can be attributed to insufficient refinement downstream the cylinder in Mesh3.

Table 2

Comparison between the maximum value of the components of velocity, of pressure, and of the Cartesian components of elastic stress at $Ws = 2$ reported by Sun et al. [21] and computed on Mesh3 with $h^u = 0.01$, $\eta_a = 1$

Field	Sun et al. [21]		Mesh3		$\Delta_{\max}$	$\Delta_{\min}$	$\Delta_{\max}(\%)$	$\Delta_{\min}(\%)$
	Maximum	Minimum	Maximum	Minimum				
v_1	1.6475	0.0000	1.6484	0.0000	−0.0009	0.0000	−0.05	0.00
v_2	0.4523	−0.4363	0.4525	−0.4396	−0.0002	0.0033	−0.05	−0.76
p	10.4290	0.0000	10.4050	0.0003	0.0240	−0.0003	0.23	0.00
σ_{11}	9.8994	−0.1304	17.2733	−0.1283	−7.3739	−0.0021	−54.27	1.63
σ_{12}	3.0102	−2.1824	3.0381	−2.2120	−0.0279	0.0296	−0.92	−1.35
σ_{22}	5.7430	−0.1326	5.7617	−0.1324	−0.0187	−0.0002	−0.33	0.14

$\sigma_{ij} \equiv (\eta_p/\lambda)(M_{ij} - \delta_{ij})$. The agreement of all values is excellent, except for the maximum value of the streamwise normal elastic stress σ_{11} in the wake of the cylinder, which differs by 54%.

8.1.2. Portraits of flow characteristics and molecular properties at $Ws = 2$

At $Ws = 2$ the streamlines differ only slightly from the Newtonian pattern. The highest rate of strain is attained at the waist of the cylinder, where the distance between the cylinder and the channel wall is smallest. Fig. 5 (top) shows contours of molecular extension and shear rate, defined in Section 7.2. The molecular extension rate is the highest near the upstream stagnation point on the cylinder, where the molecules orient perpendicular to the stagnation streamline and stretch across and contract along the upstream stagnation streamline; and in the wake of the cylinder by the downstream stagnation point, where the molecules stretch and orient along and contract across the stagnation streamline. The molecular shear rate is the highest at the waist of the cylinder, where the rate of strain is the highest.

Fig. 5 (bottom) shows the eigenvalues of the conformation dyadic—the squared molecular stretches. On the upstream stagnation streamline, the molecules contract in the streamwise direction and stretch in the cross-stream direction. The molecules are most distorted in the wake downstream of the cylinder; the highest molecular distortion is 14.66 and occurs 0.912 cylinder radii downstream of the cylinder. The molecules shrink first in the cross-stream direction, then elongate in the streamwise direction as they depart the downstream stagnation point and traverse the wake of the cylinder. The high values of molecular distortion computed are partly due to the extreme molecular compliance built into the Oldroyd-B equation. The Oldroyd-B equation yields a degenerate behavior in uniaxial as well as planar steady extensional flow, where it predicts infinite stresses at finite value of the Weissenberg number, $Ws = 1/2$ ([36], p. 26); in the computation at $Ws = 2$ on the finest mesh, the flow at the midplane in the cylinder's wake is planar extensional, and the local Weissenberg number λL_{11} exceeds the critical value 1/2 in the third element downstream of the cylinder ($x_1 \approx 1.033R$), where the convective term is small ($v_1 \approx 0.0049Q/h$) and thus the behavior of the equation approaches that of steady flow.

The Oldroyd-B model is built by assuming that polymer molecules follow sudden imposed strains and relax at a rate which is linearly proportional to their stretch: these hypotheses approximate poorly the behavior of strongly stretched and oriented molecules, and the computed distributions of molecular stretch shown in Fig. 5 likely overpredict the distributions of stretch that a real solution of flexible polymer coils would attain.

8.2. Downstream section of a slot coater

The equation system describing the flow of a Newtonian liquid in the downstream section of a slot coater was solved to test the correctness of the mesh generation equations and the free surface boundary conditions. The Galerkin/finite element solution was computed as the flow of a polymer solution with no elasticity, i.e. Eqs. (22)–(24) were solved with the constitutive Eq. (8) of the total stress, (10) of the elastic stress, together with $a = 0$, and (21) of the viscous stress, with $\eta_a = \mu = 1$. Fig. 6 shows the flow domain and the boundary conditions used.

Four test cases were chosen to compare the results with those of Silliman [48]: (1) $Q = 0.3, Re = 0, Ca = 0.1$; (2) $Q = 0.5, Re = 0, Ca = \infty$; (3) $Q = 0.5, Re = 10, Ca = \infty$; (4) $Q = 0.7, Re = 0, Ca = \infty$; where $Re \equiv \rho v L/\mu$ is the Reynolds number, $Ca \equiv \mu v/\varsigma$ is the capillary number, and Q is the flow rate per unit width of the slot. The unit of velocity v is the web speed, and the unit of length L is the height of the gap between the slot die and the web.

The sensitivity of the flow to location of the open boundaries upstream and downstream was assessed by doubling the upstream and downstream length of the flow domain. The solutions computed on the two domains agreed to within 0.04%; therefore, all subsequent solutions were computed on the shorter

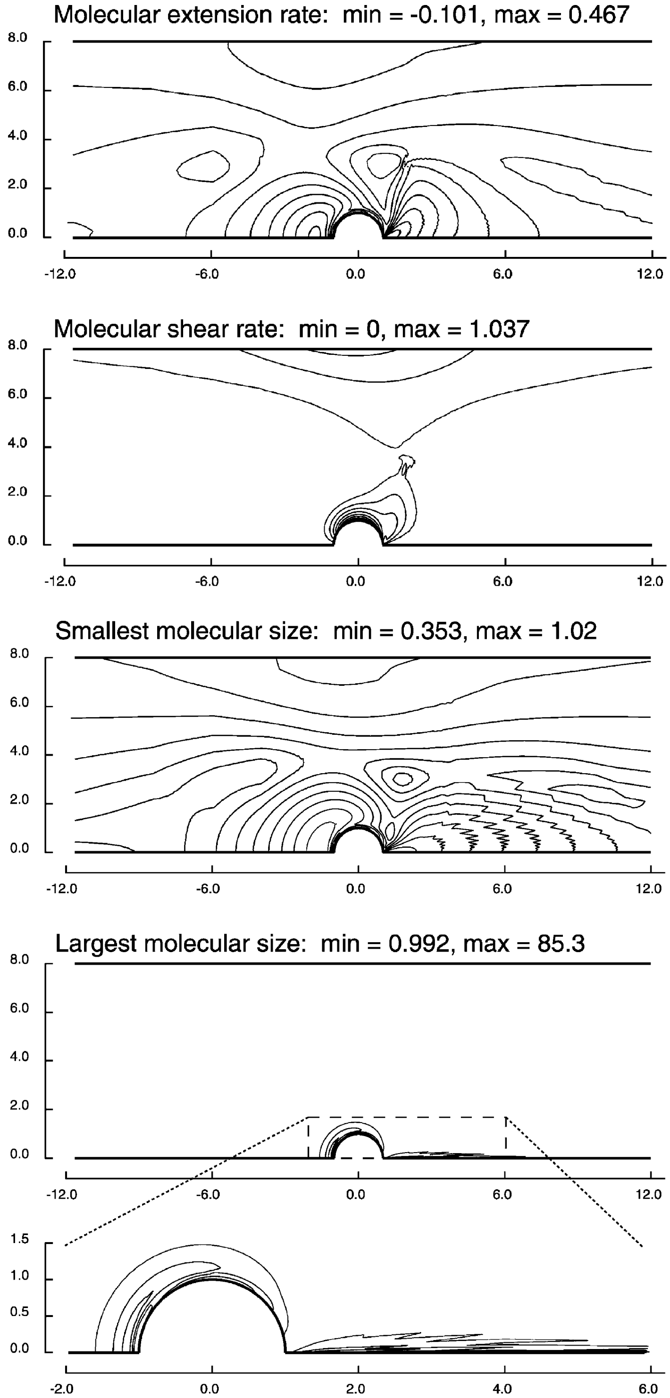

Molecular extension rate: min = -0.101, max = 0.467

Molecular shear rate: min = 0, max = 1.037

Smallest molecular size: min = 0.353, max = 1.02

Largest molecular size: min = 0.992, max = 85.3

Fig. 5. Top to bottom: Molecular extension rate $\dot{\varepsilon}_M$, shear rate $\dot{\gamma}_M$, smallest eigenvalue, and largest eigenvalue of the conformation dyadic. 11 equally spaced contour lines are plotted; lighter shades of gray denote lower values of the variables. Mesh3, $Ws = 2$, $h^u = 0.01$, $\eta_a = 1$.

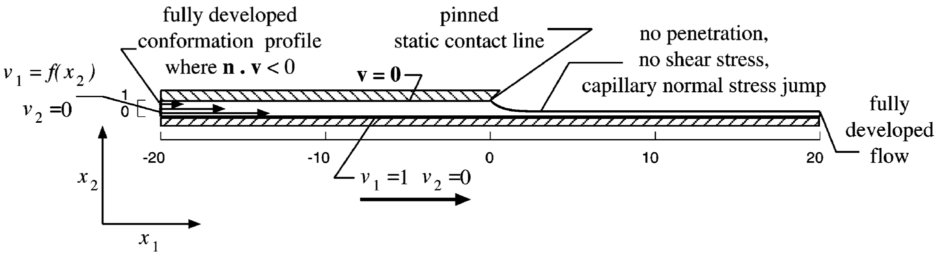

Fig. 6. Flow domain and boundary conditions used in analyzing the flow of a Newtonian liquid in the downstream section of a slot coater.

computational domain. The meshes had 792 elements and 15,580 degrees of freedom. The test case $Q = 0.5$, $Re = 0$, $Ca = \infty$ was also run on a refined mesh with 2736 elements and 52,948 degrees of freedom. Spot checks of local values of pressure and free surface shape revealed differences of less than 10^{-4} between the two meshes.

Fig. 7 compares the computed shapes of the free surfaces and pressure profiles along the moving web to those reported by Silliman ([48], Fig. F10). The difference between the profiles is approximately equal to the accuracy achieved in reading Silliman's Fig. F10 (1% of the full scale).

The computed pressure at the inflow plane under the slot is lower than the pressure outside the free surface by 1.5506 viscous units when $Q = 0.5$, $Re = 0$, and $Ca = \infty$. In these conditions, the lubrication approximation predicts that the pressure under the slot should match that outside the free surface. It is not so because the free surface is stretching just downstream of the static contact line; because the liquid is incompressible, the velocity gradient along the free surface induces a velocity gradient normal to the free surface, which in turn generates a small but non-zero viscous normal stress and lowers the pressure under the free surface close to the contact line. The pressure gradient vanishes under the slot, and the pressure starts rising towards the ambient pressure approximately 0.5 gapwidths upstream of the static contact line.

Conversely, if the same pressure value is specified at the inflow boundary and outside the free surface—and consequently the flow rate is not fixed, as in a knife coater—the film thickness h_∞ exceeds the half-gap at $Re = 0$, and $Ca = \infty$. The computed value of $h_\infty/L = 0.5065$ depends on the distance of the inflow boundary from the static contact line, which sets the magnitude of the pressure gradient.

Solving the lubrication equations yields coarser approximations to the flow field than solving the Navier–Stokes system; thus, the predictions of the lubrication equations cannot be used as stringent tests of the correctness of Petrov–Galerkin/finite element solution procedures, although they are useful when comparing approximate trends.

9. Premetered slot coating flow with recirculation, infinitely dilute solutions

The flow of an ultra-dilute ($c_p \approx 0$) polymer solution in the downstream section of a slot coater was computed by setting $G = \rho c_p kT = 0$ in the expression of the free energy; in this situation the evolution equation of conformation decouples from the mass and momentum balances. The shape of the flow domain and the boundary conditions are shown in Fig. 6. The inflow boundary was placed 20 gapwidths h upstream of the static contact line; spot checks showed that placing the inflow boundary

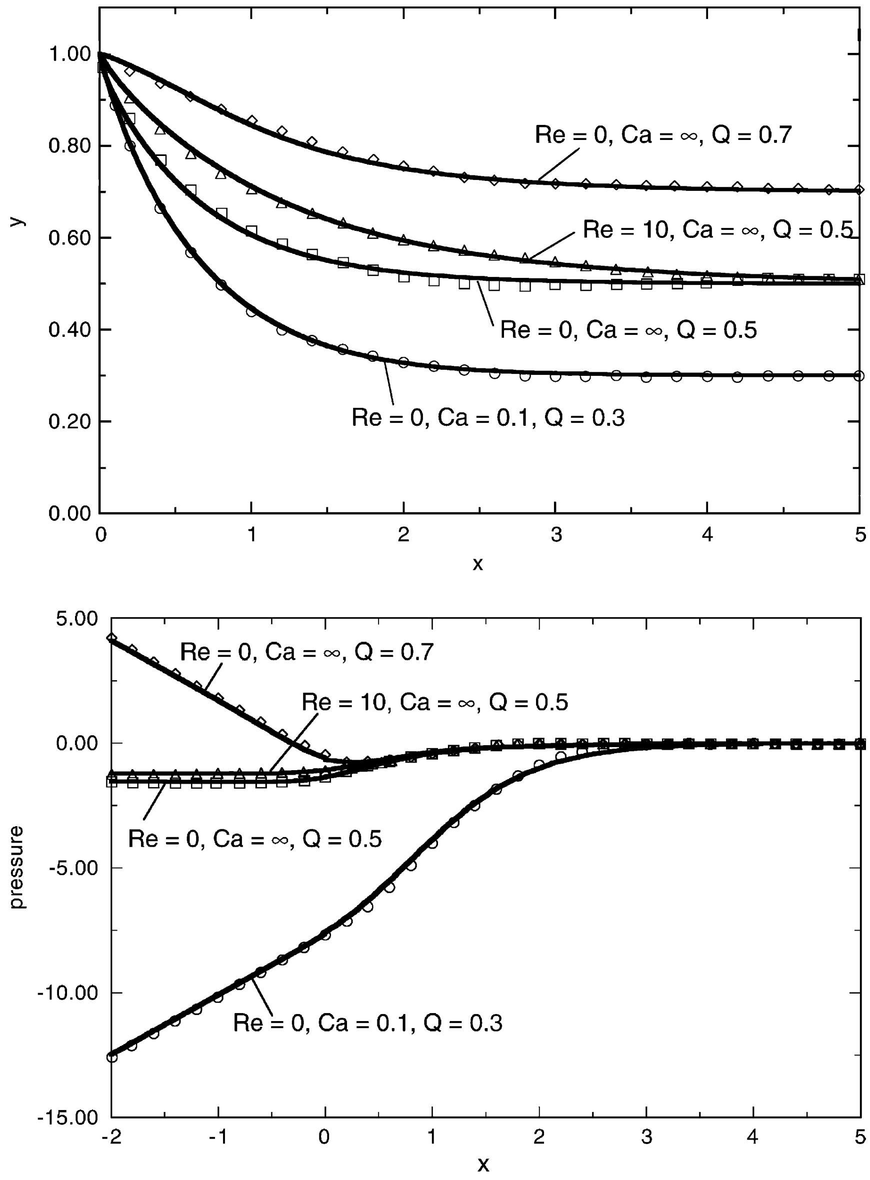

Fig. 7. Comparison of free surface shapes (top) and pressure profiles on the web (bottom) in the downstream end of a slot coater. The solid lines were computed; the symbols were read from Fig. F10 of Silliman [48] with datathief (NIKHEF-K).

only 15 gapwidths upstream of the contact line yielded the same flow and distributions of conformation were not affected.

Premetered flows were computed by imposing a fully developed velocity profile. No-slip was imposed at solid boundaries, and the web speed was used as characteristic velocity. No-penetration and the capillary force balance were imposed at the free surface. The flow was taken to be fully developed at the outflow boundary ($\boldsymbol{n} \cdot \nabla \boldsymbol{v} = 0$). The position of the static contact line was fixed.

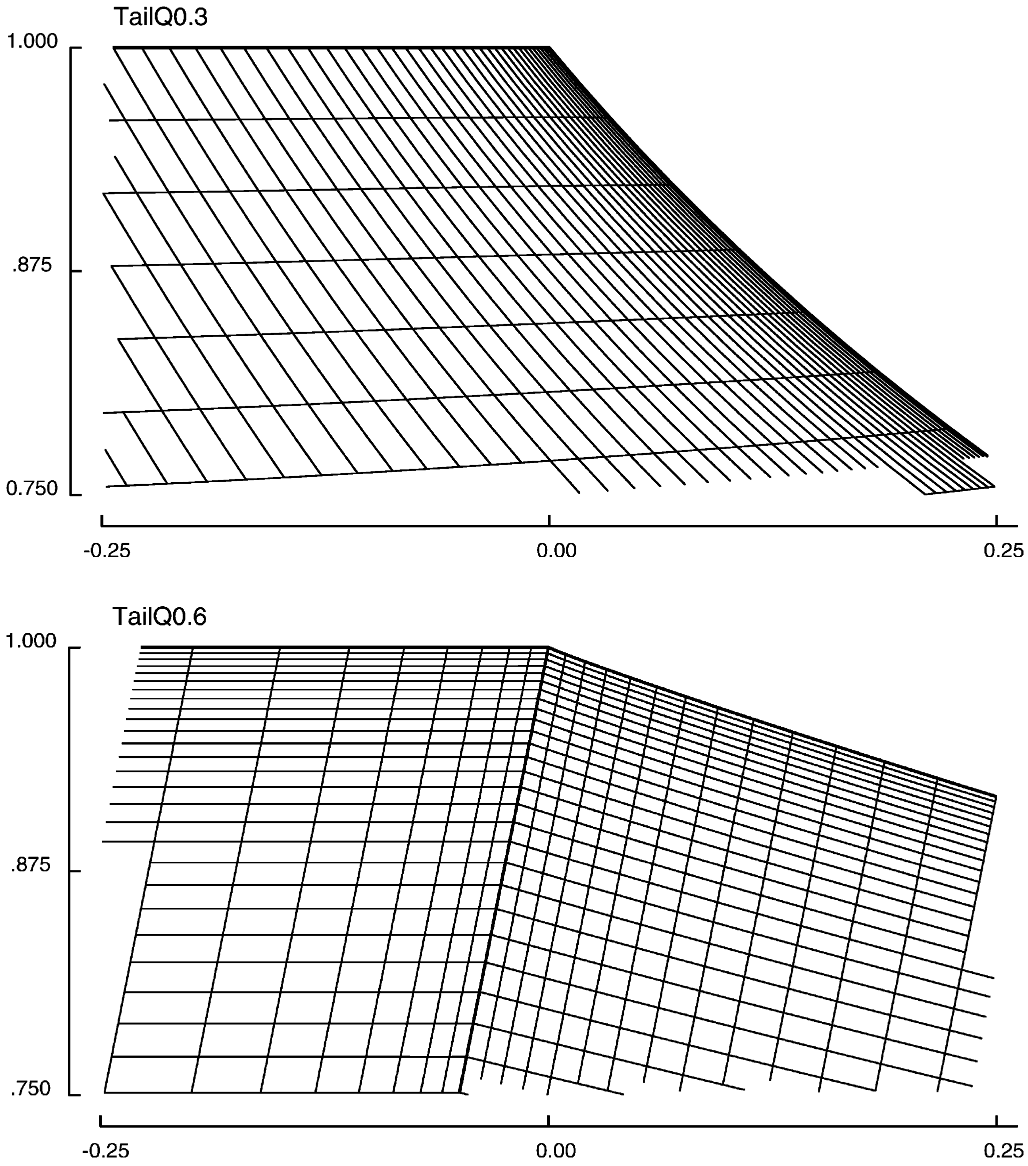

Fig. 8. Detail of the static contact line region of the finite element tessellations used to study the flow of polymer solutions in the downstream section of a slot coater with a recirculation (top) and without a recirculation (bottom).

The dimensionless numbers were $Q = 0.3$, at $Ca = 0.1$ and $Re = 0$. The finite element tessellation had 3456 elements strongly concentrated under the free surface to capture the layer of conformation that arise there at high Weissenberg number (top of Figs. 8 and 9 and Table 3). Analyzing the flow of an ultra-dilute solution is interesting because it allows a direct comparison of different models of polymer behavior under the same non-trivial kinematics; such flows are expected to occur, for example, in flows of ultra-dilute DNA solutions (e.g. [9,49,50]).

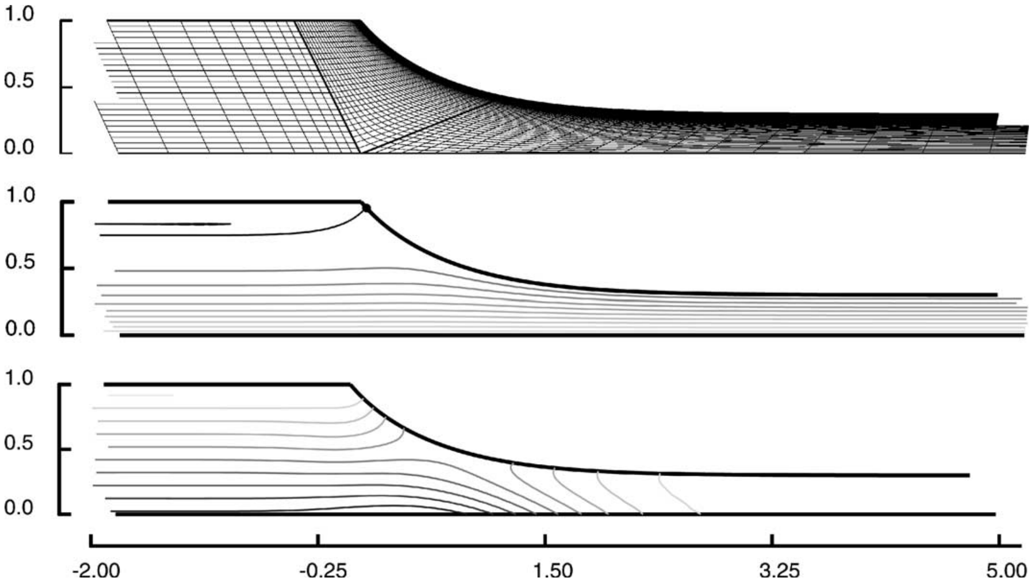

Fig. 9. From top to bottom: detail of the finite element tessellation, streamlines and of the positive eigenvalue of the rate of strain. Downstream section of a slot coater with a recirculation. The stagnation point on the free surface is marked with a small circle in the streamline plot. Imposed flow rate $Q = 0.3$, Reynolds number $Re = 0$, capillary number $Ca = 0.1$.

9.1. *Flow kinematics*

The computed streamlines are shown in Fig. 9; a stagnation point is present on the free surface, and the separating streamline is shown that divides the liquid caught in the recirculation from that entrained by the moving web.

Fig. 9 also shows the contours the scalar rate of strain—the positive eigenvalue of the rate of strain dyadic. $\boldsymbol{L}$ is exactly traceless everywhere in the flow; the maximum value of $\mathrm{Tr}\,\boldsymbol{L}$ computed with the usual equation $\nabla \boldsymbol{v} - \boldsymbol{L} = 0$ in place of Eq. (19) was 0.0035. The highest scalar rate of strain is 1.1908 v/h; it occurs on the web 0.406 gapwidths downstream the static contact line. According to Richardson's analysis [51], the velocity gradient grows without bound as the static contact line is approached. The components of the interpolated velocity gradient $\boldsymbol{L}$ along the die wall display small undershoots and overshoots in the proximity of the contact line—up to 0.015 v/h on the die wall approximately $10^{-3}h$

Table 3
Elements and unknown basis function coefficients of the finite element meshes used to analyze the downstream section of a slot coater with (TailQ.03) and without (TailQ0.6) recirculation

Mesh	Elements	Unknown basis function coefficients					
		$\boldsymbol{x}$	$\boldsymbol{v}$	p	$\boldsymbol{L}$	$\boldsymbol{M}$	Total
TailQ0.3	3456	28,178	28,178	10,368	14,356	14,356	94,436
TailQ0.6	4320	35,114	35,114	12,960	17,836	17,836	118,860

upstream of the static contact line; the overshoot grows larger and occurs on a smaller length scale as the mesh is refined close to the contact line, as observed by Salamon et al. [52] too. However, the overshoot is small because the velocity gradient vanishes at the stagnation point on the free surface and the stagnation line is close to the contact line; such a small overshoot of L_{ij} does not affect the computation of the polymer conformation. This is not the case when the recirculation under the wall is absent, as discussed in Section 10 below.

The distributions of polymer conformation in the flow were computed by solving the transport equation of $\boldsymbol{M}$ with the Oldroyd-B (affinely deforming), FENE-P with $b = 100$ (extensible) and $b = 10$ (semiextensible), and Larson semirigid ($\xi = 0.1$) and rigid ($\xi = 0$) models.

Fig. 10 shows the largest (top), smallest in-plane (middle), and smallest out-of-plane (bottom) eigenvalues of the conformation dyadic in the flow. At $Ws \lesssim 1$, the affinely stretching Gaussian segments and the extensible and semiextensible FENE-P segments are stretched and oriented to a comparable degree, whereas the semirigid and rigid segments are much less stretched. The effects of the finite extensibility of the semiextensible segments become important at $Ws \approx 1$, those of the extensible segments at $Ws \approx 2$.

Because none of the models used here sets a non-zero lower bound on it, the smallest eigenvalue of conformation becomes dangerously close to vanishing in regions of extensional flow. The minimum out-of-plane eigenvalue m_2 of the rigid and semirigid molecules departs from its equilibrium value at very low Weissenberg number because the rate of strain $\boldsymbol{D}$ enters the equation of change of m_2 directly through the partially stretching derivative. If the molecules are extensible or semiextensible, the out-of-plane eigenvalue is close to its equilibrium value at higher Weissenberg number because m_2 is uncoupled from the in-plane rate of strain, and is driven out of equilibrium by a transversal molecular contraction due to the finite extensibility of the molecules. At finite concentration, such transversal molecular contraction would induce additional spanwise compressive stresses, which could affect the stability of the flow to spanwise perturbations. The curves terminate where there appeared to be no solution with a positive definite conformation everywhere in the flow (Table 4).

9.2. Portraits of molecular conformation

The computed distributions of polymer stretch are reported here at $Ws = 3$. Fig. 11 shows contour lines of the eigenvalues of the conformation dyadic in the flow.

At $Ws = 3$, the Gaussian, extensible, and semiextensible molecules, are mainly extended under the stretching section of the free surface, immediately downstream of the region of the highest molecular

Table 4
Downstream section of a slot coater, flow with recirculation

Model	$Ws^{\max}$	$m_3^{\max}$	$m_1^{\min}$	$m_2^{\min}$
Affine Gaussian	3.551	854.9	5.03×10^{-2}	–
FENE-P, $b = 100$	6.331	258.8	5.13×10^{-2}	1.66×10^{-1}
FENE-P, $b = 10$	9.789	27.46	4.34×10^{-2}	9.47×10^{-2}
Retracting, $\xi = 0.1$	22.78	13.36	1.97×10^{-2}	4.41×10^{-2}
Rigid, $\xi = 0$	76.53	2.982	2.03×10^{-3}	1.20×10^{-2}

Maximum Weissenberg number attained $Ws^{\max}$, maximum in-plane conformation eigenvalue $m_3^{\max}$, and minimum in-plane $m_1^{\min}$ and out-of-plane $m_2^{\min}$ conformation eigenvalues predicted with different models of polymer behavior. $Q = 0.3$, $Re = 0$, $Ca = 0.1$.

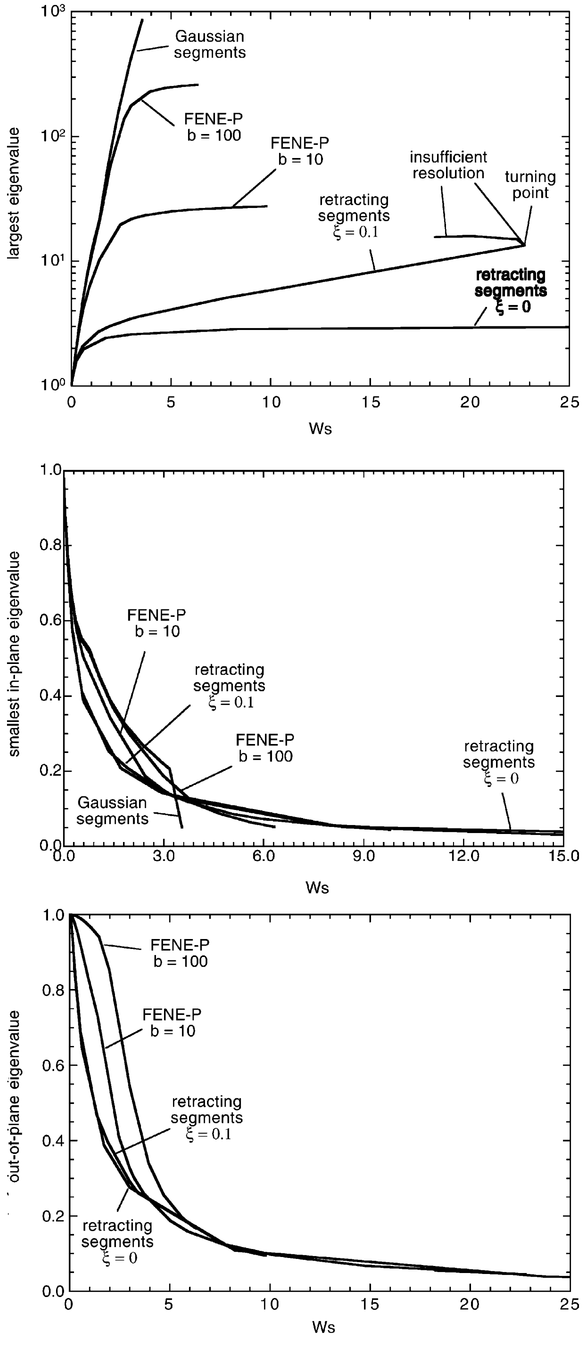

Fig. 10. Maximum in-plane eigenvalue ($m_3^{\max}$), minimum in-plane ($m_1^{\min}$) and minimum out-of-plane ($m_2^{\min}$) eigenvalues of conformation vs. Weissenberg number $Ws \equiv \lambda v/h$ in the flow in the downstream section of a slot coater with a recirculation, predicted with different models of polymer behavior. The turning point in the continuation path computed with the semirigid, partially retracting segments model coincides with the failure of the mesh to capture the steep conformation layer which is arising under the free surface at $Ws \approx 20$. $Q = 0.3$, $Re = 0$, $Ca = 0.1$.

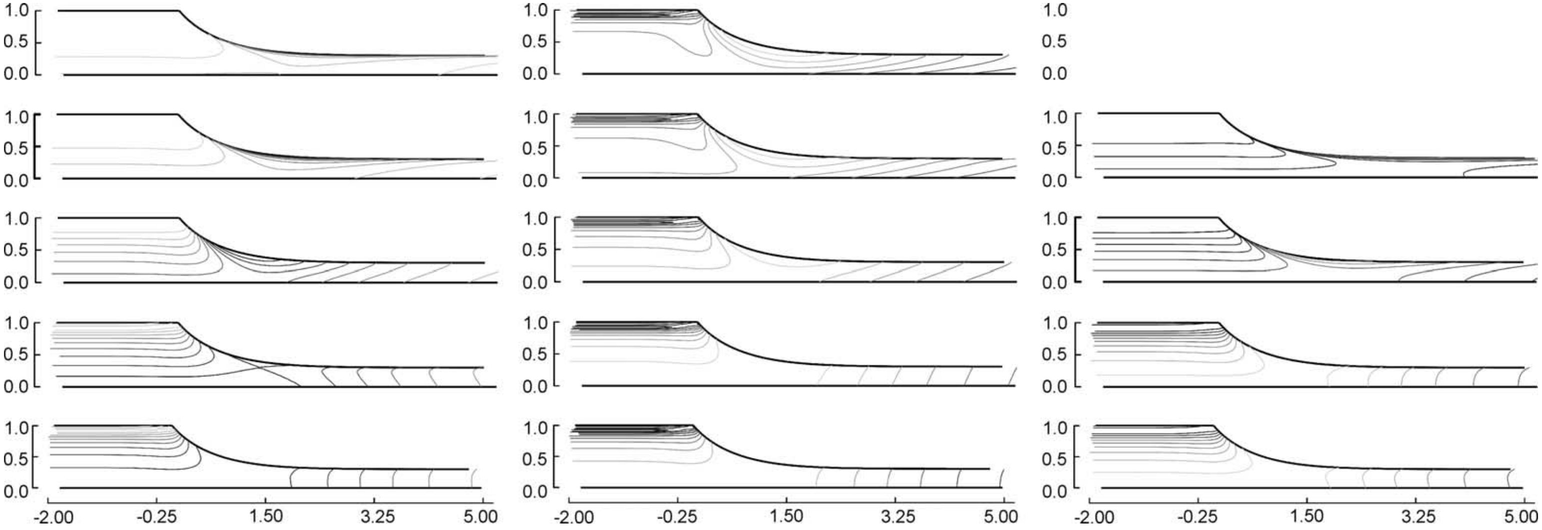

Fig. 11. Detail of the contours of the largest (left, m_3), smallest (center, m_1) in-plane, and out-of-plane (right, m_2) eigenvalue of the conformation dyadic in the downstream section of a slot coater with a recirculation. From top to bottom: affine Gaussian segments (Oldroyd-B); FENE-P extensible ($b = 100$) and semiextensible ($b = 10$) segments; semirigid, partially retracting ($\xi = 0.1$) segments; and rigid ($\xi = 0$) rods. $Q = 0.3$, $Re = 0$, $Ca = 0.1$, $Ws = 3$.

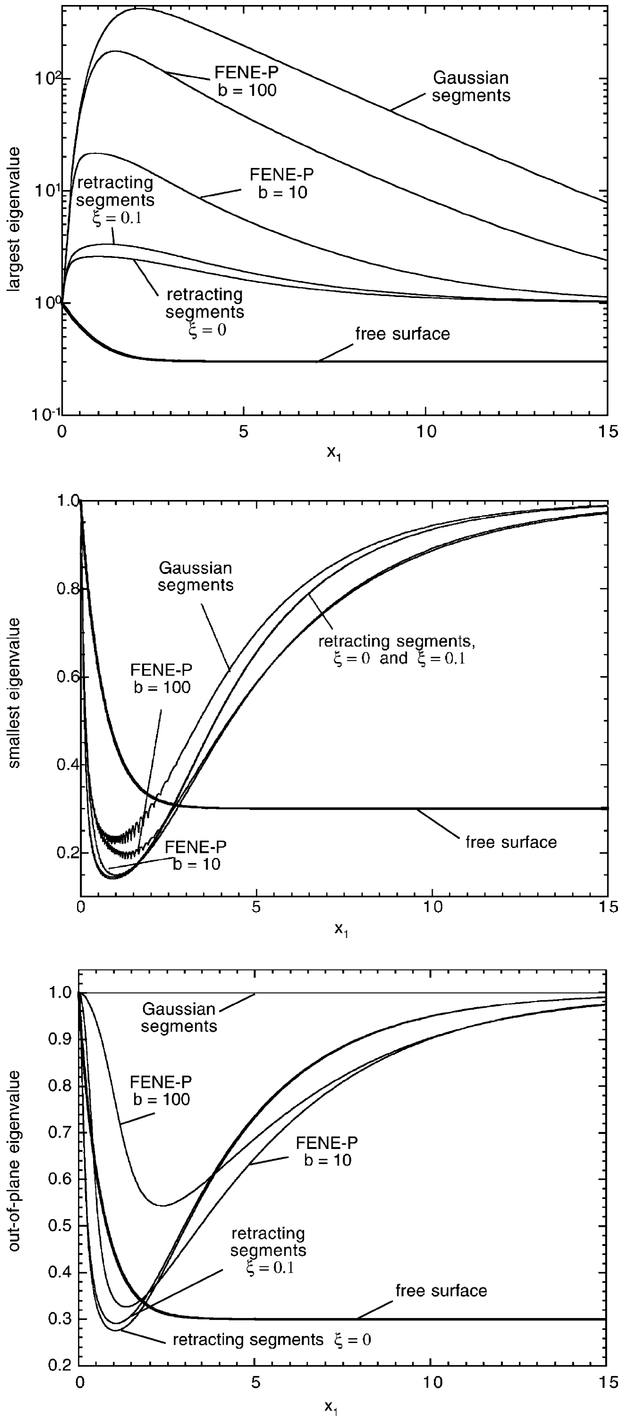

Fig. 12. Largest (m_3) and smallest (m_1) in-plane and out-of-plane m_2 eigenvalues of the conformation dyadic at the free surface of the downstream section of a slot coater with a recirculation, predicted with different models of polymer behavior: affine Gaussian segments (Oldroyd-B); FENE-P extensible ($b = 100$) and semiextensible ($b = 10$) segments; semirigid, partially retracting ($\xi = 0.1$) segments; and rigid ($\xi = 0$) rods. $Q = 0.3$, $Re = 0$, $Ca = 0.1$, $Ws = 3$.

extension rate (Fig. 14). The layer of conformation is steepest in the flow of Gaussian molecules. The semirigid and rigid molecules are stretched under the free surface (Fig. 11, left), where the scalar rate of strain is lower (Fig. 9) but the straining is persistent (Fig. 14) because the rate of strain dyadic and the conformation dyadic rotate together, and at the web, where the scalar rate of strain is the highest (Fig. 9) but the polymer segments are not aligned with the rate of strain dyadic.

At lower Weissenberg number, the molecular stretch m_3 computed with all models of molecular behavior is highest at the web; the stretch computed with the semirigid and rigid models becomes highest at the free surface at higher Weissenberg number.

The eigenvalues of conformation along the free surface are shown in Fig. 12, together with the free surface profile. The highest molecular stretch along the free surface predicted by the affine Gaussian

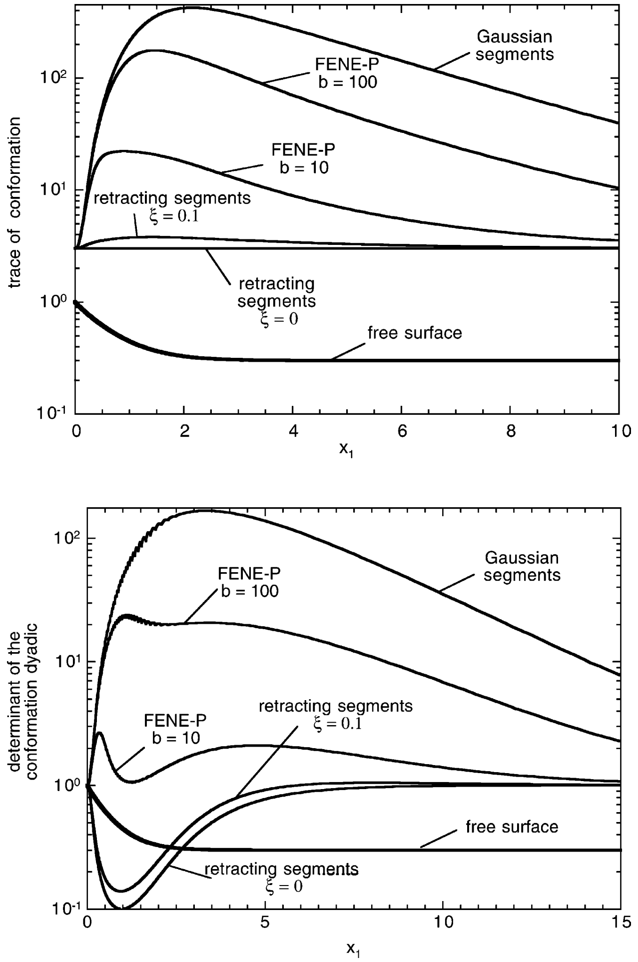

Fig. 13. Trace and determinant of the conformation dyadic at the free surface of the downstream section of a slot coater with a recirculation, predicted with different models of polymer behavior: affine Gaussian segments (Oldroyd-B); FENE-P extensible ($b = 100$) and semiextensible ($b = 10$) segments; semirigid, partially retracting ($\xi = 0.1$) segments; and rigid ($\xi = 0$) rods. $Q = 0.3$, $Re = 0$, $Ca = 0.1$, $Ws = 3$.

segments model is over 100 times larger than that predicted by the rigid rod model. The behavior of the smallest eigenvalue parallels that of the largest eigenvalue, although it is more difficult to capture the value of the smallest eigenvalue than it is to approximate the value of the largest eigenvalue of conformation (see [9] for details).

Fig. 13 shows the trace and the determinant of the conformation dyadic along the free surface. If the molecules are extensible or semiextensible, the trace of the conformation is dominated by its largest eigenvalue and parallels closely its trend. As expected, the trace of the conformation dyadic is constant everywhere if the molecules are rigid. The determinant of the conformation dyadic of the affine Gaussian segments grows steadily on the free surface. If the molecules are finitely extensible a dip appears in the profiles of det $\boldsymbol{M}$, although the flowing molecules are effectively larger than at equilibrium (det $\boldsymbol{M} \geq 1$) under the free surface in this case. Conversely, the semirigid and rigid molecules are effectively smaller during the flow because they orient without stretching appreciably.

9.3. Distributions of molecular extension and shear rates

Fig. 14 shows the contour lines of the distributions of molecular extension rate $\dot{\varepsilon}_{\boldsymbol{M}}$ defined by Eq. (33) and molecular shear rate $\dot{\gamma}_{\boldsymbol{M}}$ defined by Eq. (34). The molecular extension rate is highest at the free

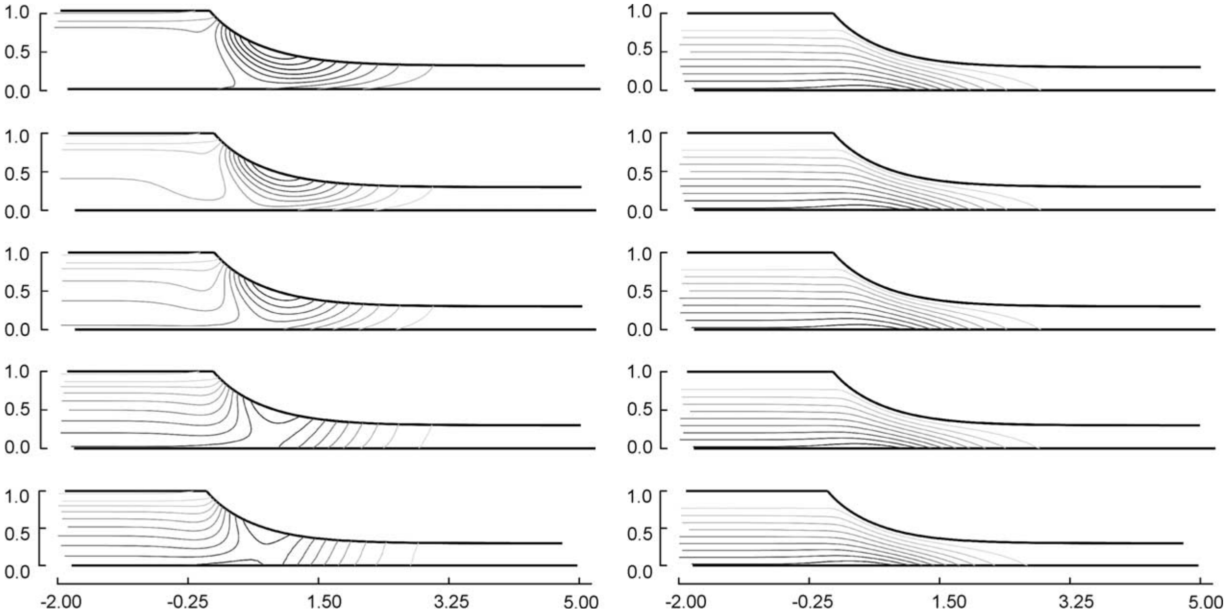

Fig. 14. Detail of the contours of the molecular extension rate $\dot{\varepsilon}_{\boldsymbol{M}}$ (left) and shear rate $\dot{\gamma}_{\boldsymbol{M}}$ (right) in the downstream section of a slot coater with a recirculation, predicted with different models of polymer behavior. From top to bottom: affine Gaussian segments; FENE-P flexible ($b = 100$) and semiflexible ($b = 10$) segments; semirigid, partially retracting ($\xi = 0.1$) segments; and rigid ($\xi = 0$) rods. Although the scalar rate of strain, i.e. the positive eigenvalue of $\boldsymbol{D}$, is highest at the web (Fig. 9 bottom), the molecular extension rate is highest and the molecular shear rate vanishes under the free surface, where the eigenvectors of the conformation dyadic are aligned with those of rate of strain. $Q = 0.3$, $Re = 0$, $Ca = 0.1$, $Ws = 3$.

surface even though the rate of strain is lower there than at the web (Fig. 9). At *Ws* = 3, the extensional character of the flow is stronger in the flows of the extensible and semiextensible molecules than in the flows of the semirigid molecules; overall, the predictions of flow type computed with the different models of polymer behavior are very similar.

The distributions of molecular stretch and molecular extension and shear rates show that at low Weissenberg number the molecules stretch predominantly near the web under the accelerating free surface (bottom of Fig. 14) where the rate of strain is highest (bottom of Fig. 9), even though the flow is dominated by shear there (Fig. 14, right). At high Weissenberg number, the molecules stretch under the free surface (top of Fig. 11), where the rate of strain is lower than in the web region, but the straining is persistent (Fig. 14, left). The transition from mild stretching induced by the shear flow at the web to the strong stretching induced by the extensional flow under the accelerating free surface occurs at lower Weissenberg number for flexible molecules, and at higher *Ws* for the rigid ones.

10. Premetered slot coating flow without recirculation, infinitely dilute solutions

The recirculation-free flow of a Newtonian liquid in the downstream section of a slot coater was computed at a dimensionless flow rate $Q = 0.6$, at $Ca = 0.1$ and $Re = 0$. The finite element tessellation

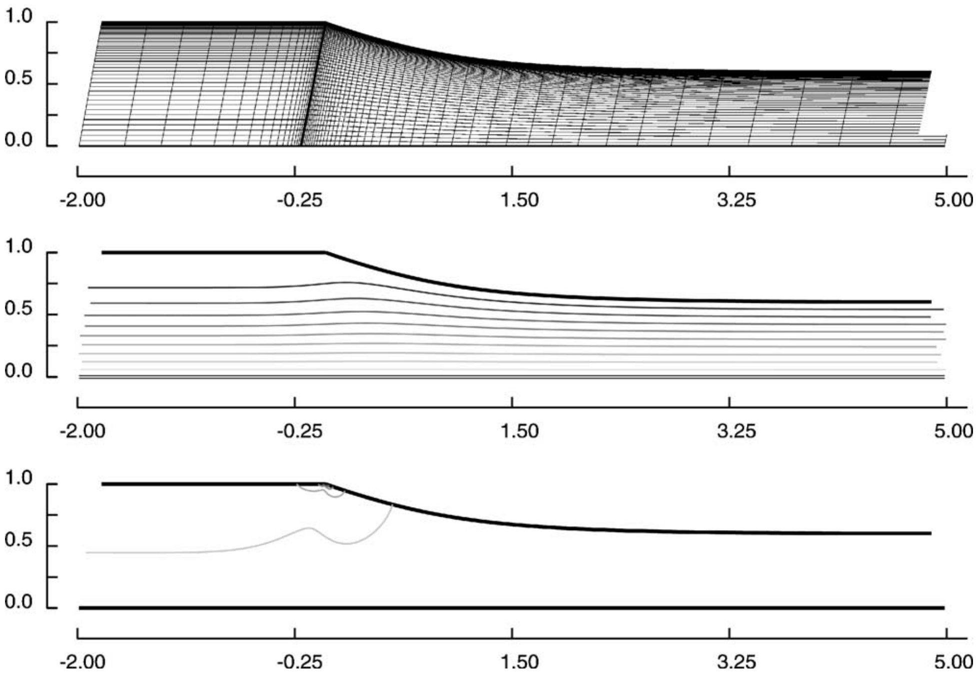

Fig. 15. From top to bottom: detail of finite element tessellation, streamlines, and of the contours of the positive eigenvalue of the rate of strain. Downstream section of a slot coater without a recirculation. Imposed flow rate $Q = 0.6$, Reynolds number $Re = 0$, capillary number $Ca = 0.1$.

had 4320 elements strongly concentrated near the static contact line to capture the high velocity gradient and the layer of conformation that arises there (Figs. 8 and 15 and Table 3).

10.1. Flow kinematics

The computed streamlines are shown in Fig. 15: the flow is recirculation-free, as expected because the coated layer thickness exceeds one-third of the gap. Fig. 15 also displays the scalar rate of strain. As in the recirculating flow, $\mathrm{Tr}\,\boldsymbol{L} = 0$ everywhere. The highest scalar rate of strain is $4.6814v/h$; it occurs exactly at the static contact line. Richardson's analysis [51] predicts that the velocity gradient grows without bound as the static contact line is approached. Unlike in the flow with a recirculation under the die lip (Section 9), here the components of the interpolated velocity gradient $\boldsymbol{L}$ along the die wall display large undershoots and overshoots in the proximity of the contact line (Fig. 16), which become more pronounced as the mesh is refined (not shown), as observed also by Salamon et al. [52–54]. The large, rapidly varying components of the velocity gradient affect strongly the computation of the polymer

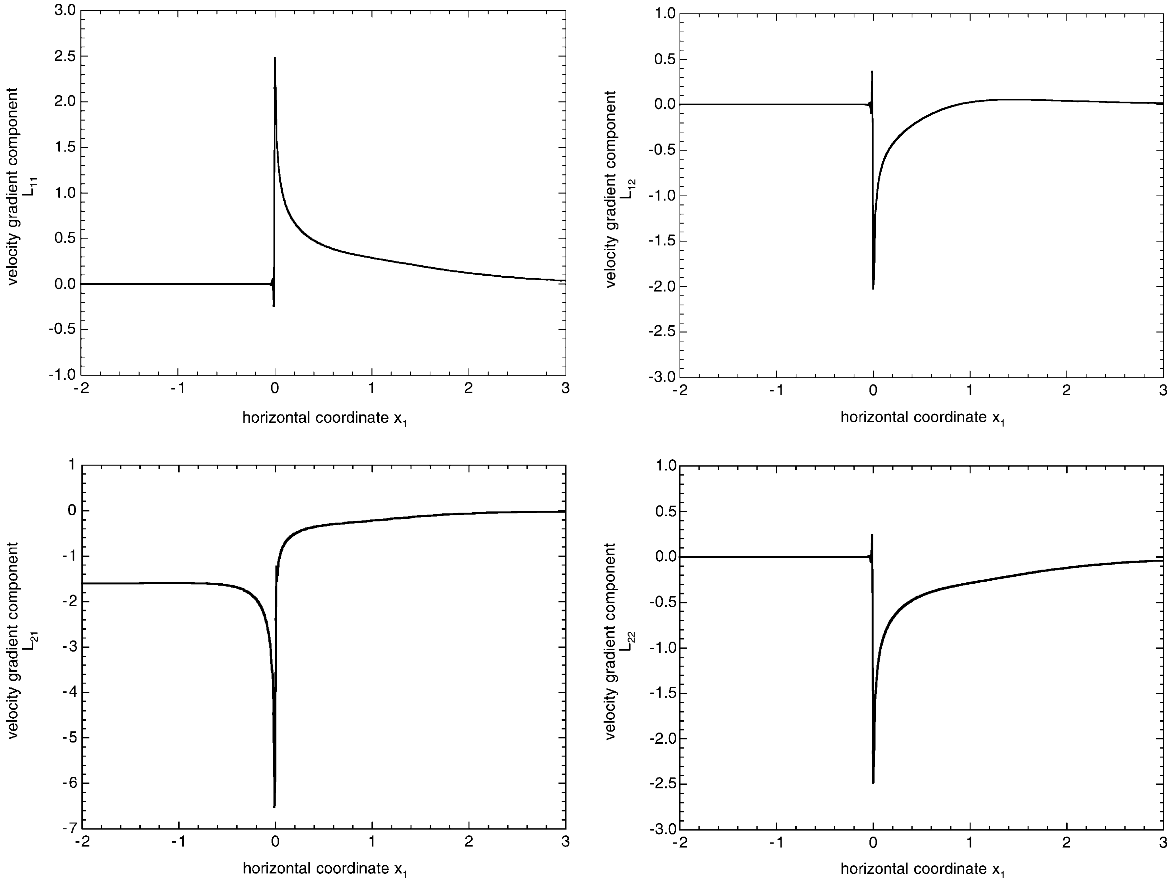

Fig. 16. Components L_{11}, L_{21}, L_{12}, and L_{22} of the interpolated velocity gradient $\boldsymbol{L}$ along the stationary die wall ($x_1 \leq 0$) and along the free surface ($x_1 > 0$) of the downstream section of a slot coater without a recirculation. $Q = 0.6$, $Re = 0$, $Ca = 0.1$.

Table 5
Downstream section of a slot coater, recirculation-free flow

Model	$Ws^{\max}$	$m_3^{\max}$	$m_1^{\min}$	$m_2^{\min}$
Affine Gaussian	0.143	16.16	0.103	–
FENE-P, $b = 100$	0.150	16.77	8.65×10^{-2}	0.955
FENE-P, $b = 10$	0.530	27.03	4.20×10^{-4}	0.182
Retracting, $\xi = 0.1$	1.159	5.623	3.22×10^{-3}	4.88×10^{-2}
Rigid, $\xi = 0$	1.442	2.966	8.73×10^{-4}	3.31×10^{-2}

Maximum Weissenberg number $Ws^{\max}$, maximum in-plane conformation eigenvalue $m_3^{\max}$, and minimum in-plane $m_1^{\min}$ and out-of-plane $m_2^{\min}$ conformation eigenvalues predicted with different models of polymer behavior. $Q = 0.6$, $Re = 0$, $Ca = 0.1$.

conformation near and at the contact line, severely limiting the maximum Weissenberg number at which a physically meaningful solution can be computed.

10.2. The high Weissenberg number limit

The distributions of polymer conformation were computed by solving the transport equation of conformation at $Q = 0.6$ and different Weissenberg numbers. Table 5 reports the highest Weissenberg number at which a solution could be computed with a positive definite conformation tensor; the computations failed to converge to such a solution at much lower Weissenberg number than in the case of the flow with a recirculation under the die lip. The conformation tensor always lost its positive definiteness at the contact line.

Fig. 17 shows the contours of the minimum eigenvalue m_1 and maximum eigenvalue m_3 of the conformation tensor computed with the affinely stretching Gaussian segments model at $Ws = 0.143$—the highest Weissenberg number at which an acceptable solution was found with this model. Each of the in-plane eigenvalues of the conformation dyadic is close to its equilibrium value in the whole flow domain, except for a narrow region near the contact line and beneath the free surface immediately downstream the contact line. The layer of conformation at the contact line cannot be resolved by refining the mesh further because doing so leads to larger overshoots and undershoots of the velocity gradient at the contact line. The distributions of conformation computed with the other four models of polymer behavior closely parallel the behavior displayed in Fig. 17; therefore they are not reported here.

Computing physically meaningful solutions of the equations of the flow of polymeric liquids when contact lines are present is challenging even when the polymer does not affect the behavior of the flow. The computational difficulty arises because the boundary condition on the momentum equation at the contact line is inappropriate, even though it does apply at a macroscopic scale if the flow is Newtonian. Changing the model of polymer behavior, i.e. the constitutive equation, merely shifts the computational problems to a different Weissenberg number dependent on the model of choice.

11. Self-metering knife coating flow with and without recirculation, dilute and semidilute solutions

The flow of dilute and semidilute solutions of affinely stretching Gaussian segments was studied by solving the coupled set of equations of the Oldroyd-B model. Although the Oldroyd-B model does not

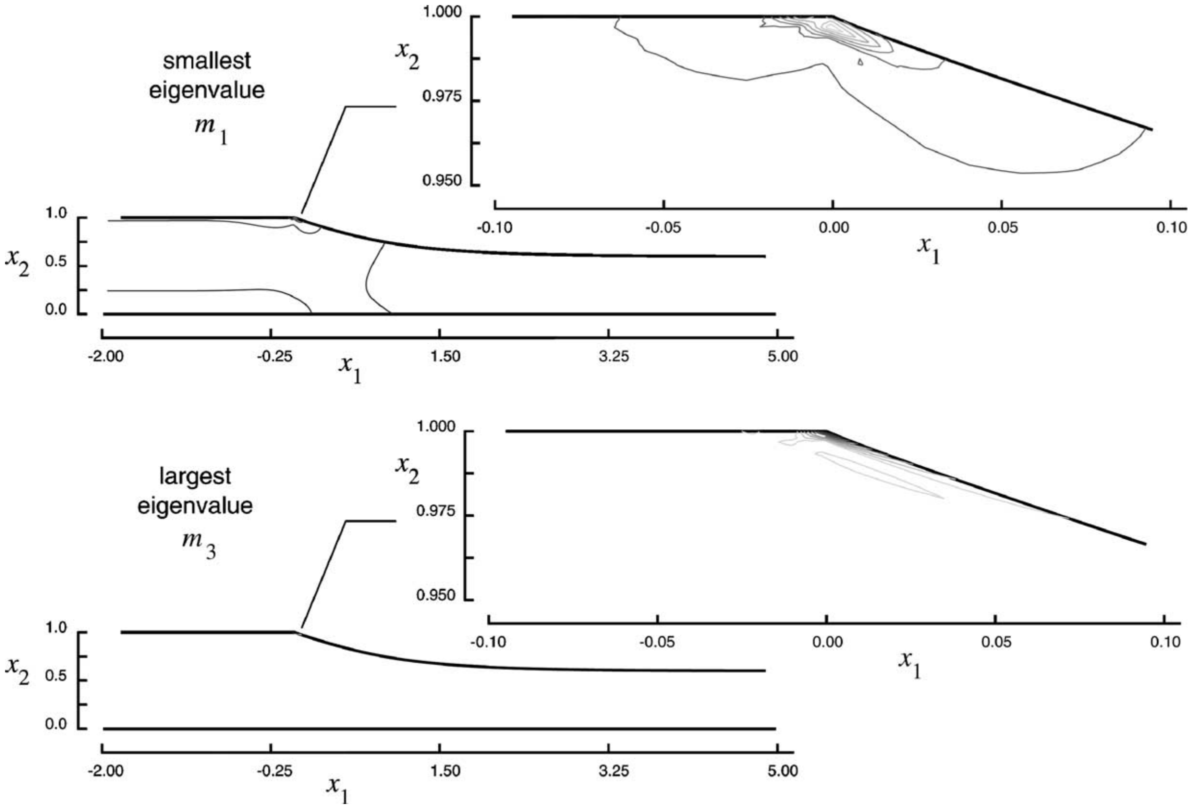

Fig. 17. Detail of the contours of the smallest in-plane eigenvalue m_1 (top) and of the largest eigenvalue m_3 (bottom) of the conformation dyadic in the downstream section of a slot coater without a recirculation, predicted with the affine Gaussian segments model. The insets show the region near the contact line. The conformation dyadic is nearly undistorted in the whole flow domain, except at the contact line. $Q = 0.6$, $Re = 0$, $Ca = 0.1$, $Ws = 0.143$.

represent adequately the non-linear behavior of any liquid, it was chosen because it predicts the most intense layers of conformation, taxing the mesh and the computational method. The results reported in this section were all computed by setting $\eta_a/\mu = 0.909$. The upwind parameter was set to $0.0787h$—approximately twice the size of the smallest element in the tessellation.

The flow was studied as a self-metering knife coating flow by imposing a fixed pressure difference between the inflow boundary and the free surface; therefore the inflow flow rate and final film thickness were computed as part of the solution of the equations of the flow. The inflow boundary was set 15.75 gapwidths upstream of the contact line; the outflow, 15.75 gapwidths downstream of the contact line. Displacing further the inflow and outflow boundaries yielded no appreciable differences in the solution in the range of parameters investigated here. The pressure at the inflow was set to $p_i = -57.7(\mu v)/h$ to have a large recirculation under the die lip in the case of Newtonian liquid, and the pressure p_a was set to zero outside the free surface.

In a real coating operation, changing the concentration or the molecular weight of the polymer can alter the polymer contribution to the viscosity, the liquids' elastic modulus, its relaxation time, or all three properties, which are related by $\eta_p \equiv G\lambda$. These three properties of the liquid enter several dimensionless

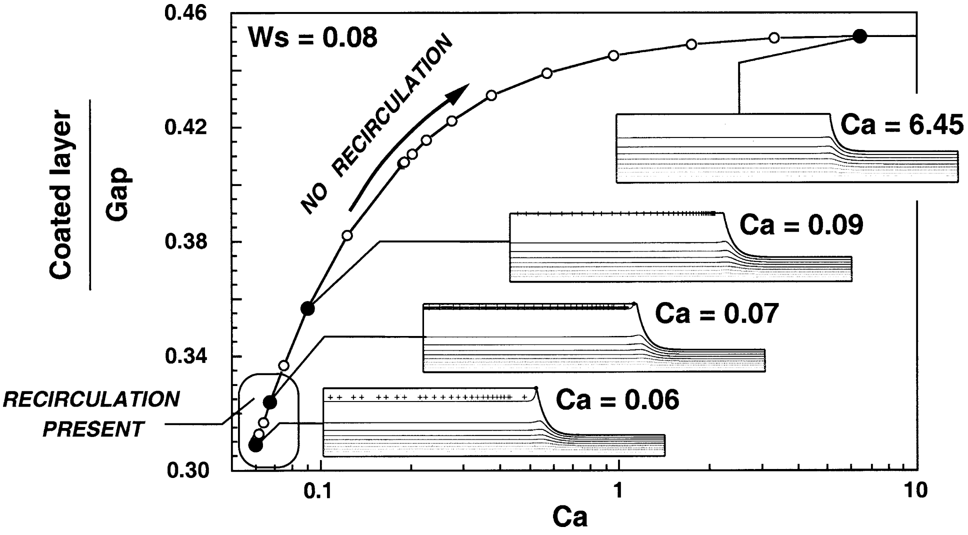

Fig. 18. Effect of polymer viscosity on the streamlines in a knife coating flow with parallel gap, as shown in the insets. The polymer viscosity appears in the definition of capillary number Ca. $Ws = 0.08$; $Ca^0 = 0.055$; $\Delta p^0 = -57.7$; $\eta_a/\mu = 0.909$; $\beta = Ca^0/Ca$. The vertical scale is enlarged in the streamline plots.

numbers; therefore if one of them is changed to mimic a varying concentration or molecular weight of the liquid, one or more dimensionless numbers change. Which dimensionless numbers were constant and which changed is discussed along with each case reported in the following.

11.1. Effect of polymer viscosity on flow microstructure at low Weissenberg number

The polymer viscosity was changed at low, constant Weissenberg number to investigate the effect of small amounts of elasticity on the flow structure. The polymer viscosity enters the ratio of solvent viscosity to total viscosity $\beta \equiv \mu/(\mu + \eta_p)$, the capillary number $Ca \equiv (\mu + \eta_p)v/\varsigma = Ca^0/\beta$, where Ca^0 is the capillary number defined in terms of the Newtonian viscosity alone, and the dimensionless pressure drop, $\Delta p \equiv (p_i - p_a)h/\left[(\mu + \eta_p)v\right] = \Delta p^0\beta$, where Δp^0 is the dimensionless pressure drop in terms of the Newtonian viscosity alone $\Delta p^0 \equiv (p_i - p_a)h/(\mu v)$.

Fig. 18 shows how flow structure and coated layer thickness change as polymer viscosity rises at fixed reference dimensionless pressure Δp^0 and reference capillary number Ca^0. At low capillary number, a small recirculation is present under the die lip. As the viscosity of the polymer grows, the thickness of the coated layer increases, and the recirculation under the die lip disappears. As expected, the recirculation disappears when the dimensionless coated layer thickness exceeds one-third, as in Newtonian liquids.

Fig. 19 shows how polymer viscosity affects the coated layer thickness at different values of the relaxation time. The results at low Weissenberg number show that the final coated thickness is lower than that of a Newtonian liquid with equivalent capillary number if the Weissenberg number is lower than approximately 1. At higher Weissenberg number, the computations converged to inadmissible solutions, i.e. the conformation tensor had a negative eigenvalue. The reason for this failure is that as the capillary number grows, the recirculation at the contact line disappears, and computing physically meaningful solutions is possible only if the Weissenberg number is low.

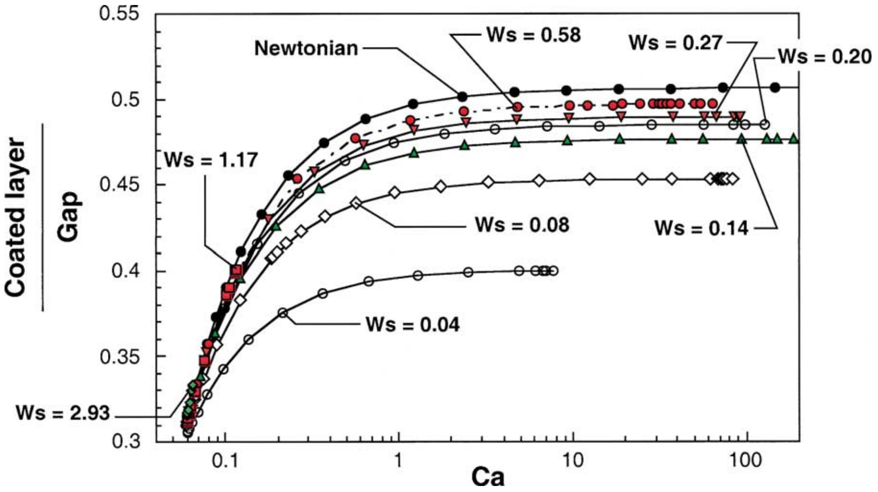

Fig. 19. Effect of polymer viscosity on thickness of coated layer delivered by a fixed pressure difference across a parallel gap knife coater at different values of polymer relaxation time. $Ca^0 = 0.055$; $\Delta p^0 = -57.7$; $\eta_a/\mu = 0.909$; $\beta = Ca^0/Ca$.

The curves at low Weissenberg number do not approach the Newtonian limit because the viscoelastic stress does not vanish at equilibrium ($\boldsymbol{\sigma} = G\boldsymbol{I}$) in the model chosen here; thus, the total normal stress on the liquid at the inflow boundary depends on the elastic modulus of the liquid and changes with the Weissenberg number—at the outflow boundary the total normal stress is set by the value of the pressure in the gas. Because the modulus $G \equiv \eta_p/\lambda$ of the liquids with the lower relaxation time is higher than the modulus of the liquids with high relaxation time, there is an excess tensile normal stress $G\int_0^h M_{11}\,\mathrm{d}x_2$ on the liquid at the inflow boundary, which induces a thinner final layer. If the total normal force were fixed, the calculations at low Weissenberg number would tend to the Newtonian limit, as expected from results obtained by perturbation theory in related problems [24].

11.2. Effect of polymer relaxation time, flow at constant viscosity

The viscosity of a polymer solution depends on the product of mass concentration ρ_p and polymer molecular weight M_w according to the Mark–Houwink relation [55] $\eta_p \sim \rho_p M_w^{\alpha}$, where α is a semiempirical exponent that depends on the quality of the solvent. The relaxation time of dilute, flexible polymer chains is proportional to the polymer's molecular weight, $\lambda \sim M_w^{1+\alpha}$. A continuation path in which the polymer relaxation time grows while the viscosity of the polymer is fixed can be visualized on Graessley's diagram [56] by using the dependence of the polymer viscosity and relaxation time on polymer concentration and molecular weight (see [9] for details). According to Graessley [56], the boundary between the dilute region and the semidilute region is a line of constant viscosity; therefore the continuation path of a sequence of cases at constant viscosity and changing molecular weight is parallel to the boundary between the dilute and semidilute regions.

In this continuation the pressure drop between the inflow section and outside the free surface was kept fixed, $\Delta p^0 = -57.7$; and the polymer relaxation time λ was raised while its modulus G was simultaneously lowered to keep the polymer viscosity $\eta_p = G\lambda$ constant. Because the gap h and the web velocity v were held fixed too, the Weissenberg number $Ws \equiv \lambda v/h$ rose with the polymer relaxation

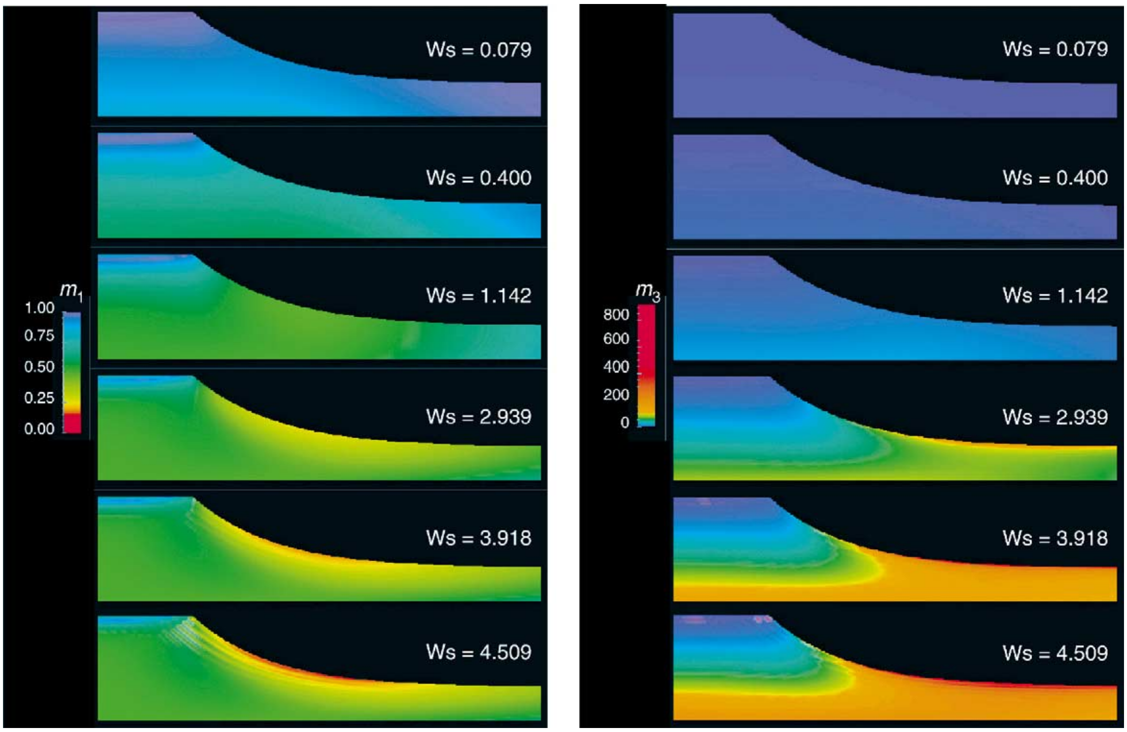

Fig. 20. Detail of the smallest (left) and largest (right) eigenvalue of the conformation dyadic at the free surface. Self-metering knife coating flow, continuation at constant polymer viscosity. $Ca = 0.06$; $\Delta p^0 = -57.7$; $\eta_a/\mu = 0.909$; $\beta = 0.917$.

time, whereas the capillary number $Ca \equiv (\mu + \eta_p)v/\varsigma$ and the ratio of Newtonian viscosity to total viscosity $\beta \equiv \mu/(\mu + \eta_p)$ stayed constant. Here $Ca = 0.06$, $\beta = 0.917$.

Fig. 20 shows the distribution of the smallest and largest eigenvalues of the conformation dyadic in the drawdown region of the flow where the layer is narrowing and the liquid near the free surface is suffering extensional strain. The shape of the free surface is almost unaffected by the Weissenberg number. At low Weissenberg number, the polymer is almost unstretched, and the highest stretch and contraction are at the moving web, where the rate of strain is the highest. As the Weissenberg number grows, the region of the highest polymer stretch and contraction moves towards the free surface, until a very steep layer of conformation arises beneath the free surface at $Ws \approx 3$.

Small wiggles in the distribution of smallest eigenvalue appear at $Ws = 3.918$, but are absent from the distribution of the largest eigenvalue; they appear there at $Ws = 4.509$; at higher Weissenberg number of the computed eigenvalues of the conformation dyadic became negative near the contact line.

11.3. *Effect of polymer relaxation time, flow at constant elastic modulus*

The elastic modulus G of dilute and semidilute–not entangled, flexible polymer chains is proportional to the polymer's molecular weight and inversely proportional to its mass concentration, $G \sim M_w/\rho_p$. Hence, a continuation path with constant elastic modulus corresponds to a line with slope of unity on Graessley's diagram [56].

Table 6
Weissenberg number $Ws = \lambda v/h$, capillary number $Ca = (\mu + \eta_p)v/\varsigma$, and ratio of Newtonian to total viscosity $\beta = \mu/(\mu + \eta_p)$ in the continuation at fixed polymer elastic modulus described in Section 11.3

Ws	Ca	β	$\dot{\gamma}^{\max}$	$m_3^{\max}$	$m_1^{\min}$
0.083	0.060	0.913	9.18	1.233	0.841
0.226	0.069	0.793	8.48	1.767	0.695
0.805	0.106	0.518	7.15	5.302	0.511
0.866	0.110	0.500	7.07	5.778	0.480
0.911	0.113	0.487	7.02	6.143	0.495
0.993	0.118	0.466	6.93	8.513	0.423

Also shown are the maximum of the positive eigenvalue $\dot{\gamma}^{\max}$ of the rate of strain $\boldsymbol{D}$; maximum of the largest and minimum of the smallest eigenvalue $m_3^{\max}$ of conformation in the flow domain.

In this continuation the reference pressure drop between the inflow section and outside the free surface was kept fixed, $\Delta p^0 = -57.7$; and the polymer relaxation time was raised while its modulus was kept constant; therefore the polymer contribution to the total viscosity rose with the relaxation time. Because the gap and the web velocity were held fixed too, the Weissenberg number Ws and the capillary number rose with the polymer relaxation time, whereas the ratio of Newtonian viscosity to total viscosity dropped (Table 6).

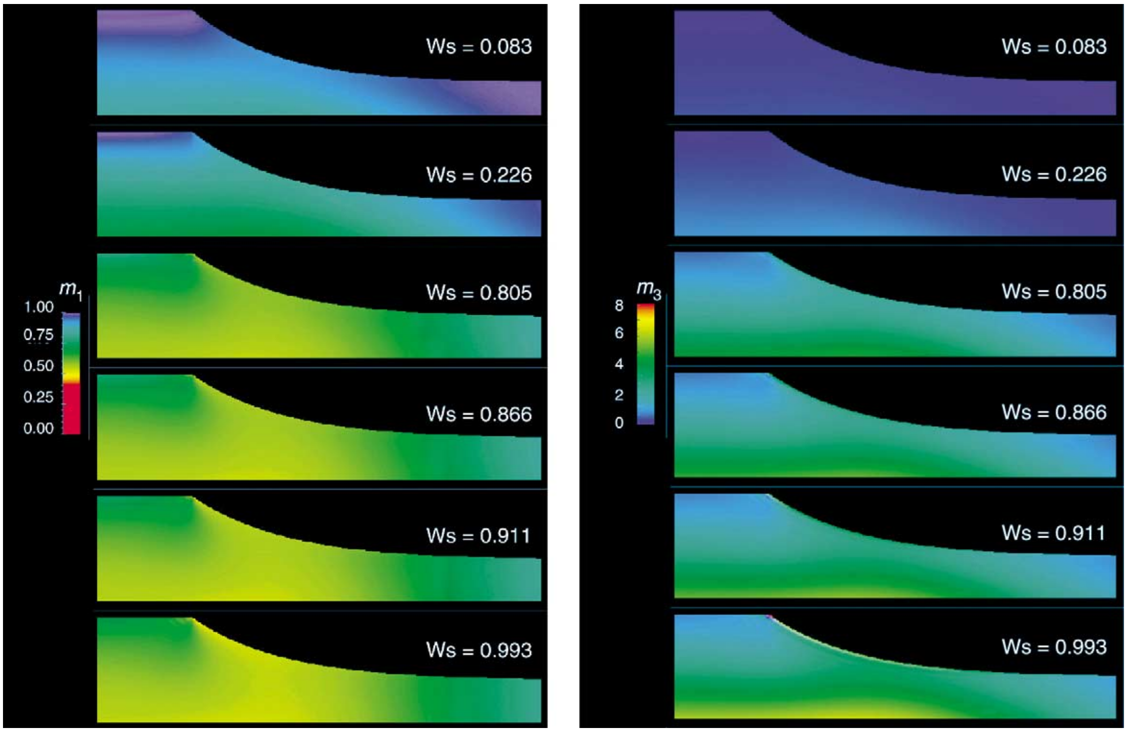

Fig. 21. Detail of the smallest (left) and largest (right) eigenvalue of the conformation dyadic at the free surface. Self-metering knife coating flow, continuation at constant polymer elastic modulus. $\Delta p^0 = -57.7$; The capillary number and the ratio of Newtonian to total viscosity corresponding to the Weissenberg numbers shown here are reported in Table 6.

Fig. 21 shows the distributions of the smallest and the largest eigenvalue of conformation at the free surface. Because the viscosity is changing during the continuation, the free surface moves outwards at high Weissenberg number, the coated layer grows thicker, and the stagnation point on the free surface moves upstream until it meets the static contact line at $Ws \approx 0.22$. The region of the highest polymer stretch moves from the web to the free surface as the Weissenberg number grows. Because the stagnation point shifts upstream, the region of the highest coil deformation moves closer to the contact line at high Weissenberg number, whereas in the continuation at constant polymer viscosity (Fig. 21) the region of the most intense stretching is one to two gapwidths downstream of the contact line. The smallest eigenvalue of conformation close to the contact line is already dangerously small at $Ws = 0.866$ (Fig. 21, left), and a very steep layer of stretching is developing at the contact line (Fig. 21, right); wiggles appear in the distribution of largest eigenvalue at the corner. No physically acceptable solution, i.e. no solution with a positive definite conformation tensor everywhere in the flow domain, was found at $Ws > 1$, almost five times lower than the limit found in the flow with no recirculation.

12. Conclusions

A computational method has been described for computing free surface flows of polymer solutions with the conformation dyadic, a variable that tracks the local average stretch and orientation of ensembles of polymer molecules. The method solves the general equations of change of conformation [6–9], which include most well-known rate-type constitutive equations previously used in theoretical modeling of flows of polymeric liquids.

The computational method combines previously published methods of computing Newtonian free surface flows [1–3,12,13,28] and viscoelastic flows with rate-type constitutive equations [4,5,18,21].

Modifications are introduced to insure that the interpolated velocity gradient is traceless, to include traction boundary conditions at free surfaces and open boundaries, and to impose inflow boundary conditions on the conformation tensor that are independent of the specific choice of constitutive model.

A new way is introduced of writing computational code that is independent of the number and type of microstructural variables, and of the particular choice of the mechanisms of change of conformation, yet retains the advantages of a full analytical Jacobian and of first-order arclength continuation in parameter space.

The suitability of the method and the correctness of the computational code are demonstrated by comparing computational results with independently obtained solutions of the equations of Newtonian and viscoelastic flows. A study of the flow of an Oldroyd-B liquid around a cylinder in a channel confirms that achieving computational results that are both mesh-independent and computational parameter-independent is very difficult at high Weissenberg number. A criterion is suggested for monitoring whether the computational results are admissible by checking that the eigenvalues of the conformation dyadic are positive at each continuation step.

The theory, computational method, and computer code prove to be very general; further work in progress has shown that the equations of the theory include a description of the behavior of elasto-viscoplastic materials based on the material's current configuration, which is particularly advantageous over the classical description based on a variable stress-free state in solving steady-state problems with open inflows and outflows [57].

The computational method was used to analyze the premetered flow of infinitely dilute solutions of polymer of varying degree of stiffness under the downstream section of a slot coater was analyzed both with and without a recirculation under the die wall, as well as the self-metering pressure-driven flow of dilute and semidilute solutions—represented by the Oldroyd-B model—beneath the downstream section of a knife coater, where the transition between recirculating and recirculation-free flow was investigated.

The solutions of the governing equations show that if a recirculation is present, the approximate value of the velocity gradient field is low in the small region between the static contact line and the stagnation point on the free surface even when the mesh is refined, although a mathematical singularity is present at the contact line. Small overshoots and undershoots of the velocity gradient are present, which do not prevent the solution of the equations of the flow at high Weissenberg number ($Ws \gtrsim 3$).

Once the recirculation is absent, the singularity at the contact line strongly affects locally the velocity gradient, which in turn affects the value of the molecular conformation dyadic there; the solutions at moderate Weissenberg number ($Ws \approx 0.15$) are unacceptable because one of the eigenvalues of the conformation dyadic is negative at the contact line, irrespective of the type of polymer model and regardless of whether the polymer is affecting the flow or not.

The equation set yields unacceptable solutions near the contact line because the boundary conditions there (no slip on the solid wall, no shear stress on the free surface) are inappropriate; these boundary conditions hold on a macroscopic scale if the flow is Newtonian. More research is needed on appropriate boundary conditions at contact lines in the flow of polymeric liquids, possibly including in the theory the migration of polymer molecules away from regions of highly stretched conformation (or high elastic stress).

When a recirculation was present under the die, the solution of the equations at high Weissenberg number lost meaning because the smallest eigenvalue of conformation became negative. None of the models of polymer dynamics known to the authors sets a non-zero lower bound on the eigenvalues of conformation. If an eigenvalue m_i associated with an eigenvector $\boldsymbol{m}_i$ vanishes, then all polymer segments must be oriented perpendicular to $\boldsymbol{m}_i$. Whether such a perfect alignment can be approached, or if a non-zero lower bound should exist on the eigenvalues of the conformation dyadic, is simply not known.

New indicators of molecular extensional rate and molecular shear rate have been introduced. They are independent of frame of reference and coordinate systems, and they are rooted in the molecular interpretation of the conformation dyadic as representative of the local average state of stretch and orientation of the molecules in the flow. These flow-type indicators indicate that the stretching at high Weissenberg number occurs under the free surface, where the straining is persistent and the molecular conformation dyadic is aligned with the rate of strain, i.e. the flow is extensional, even though the strain rate is lower there than at the web. At low Weissenberg number, the molecules stretch little, and do so near the web in the region of the highest strain rate.

Some models of polymer behavior used here predict a contraction of the conformation tensor in the spanwise direction in a two-dimensional flow which induce spanwise compressive elastic stresses that may effect the stability of the flow. If the molecules are extensible or semiextensible, this contraction occurs after the molecules stretch in the in-plane direction, and is a consequence of their finite extensibility. If they are rigid, the contraction occurs at lower Weissenberg number because it is caused by flow rather than molecular relaxation. Because current experimental evidence is inconclusive [9,58,59], it will take further experiments to answer the question of whether or not the molecular conformation tensor contracts.

Acknowledgements

Thanks are due to Prof. Marcio S. Carvalho for useful discussions on Newtonian free surface flows. This research was supported by NSF and industrial sponsors through the Center for Interfacial Engineering and by generous grants of computing time by the University of Minnesota Supercomputing Institute.

Appendix A. Formulae of the analytical Jacobian

The derivatives of the residual equations with respect to the unknown basis function coefficients are reported here together with a number of useful recurring formulae.

- Derivatives of the Jacobian of the mapping f with respect to position basis functions coefficients x_j^α:

$$\frac{\partial f}{\partial x_j^\alpha} = f \nabla_j \varphi_{\boldsymbol{x}}^\alpha \tag{A.1}$$

- Derivatives of the direct mapping deformation gradient $\boldsymbol{F}$ with respect to position basis functions coefficients x_k^α:

$$\frac{\partial F_{ij}}{\partial x_k^\alpha} = \delta_{kj} \frac{\partial \varphi_{\boldsymbol{x}}^\alpha}{\partial \xi_i} \tag{A.2}$$

- Derivatives of the inverse mapping deformation gradient $\boldsymbol{K}$ with respect to position basis functions coefficients x_j^α:

$$\frac{\partial K_{ki}}{\partial x_j^\alpha} = -K_{ji} \nabla_k \varphi_{\boldsymbol{x}}^\alpha \tag{A.3}$$

- Derivatives of the gradient of a scalar, vector component, or tensor component $\mathcal{G}$ with respect to position basis functions coefficients x_j^α:

$$\frac{\partial \nabla_k \mathcal{G}}{\partial x_j^\alpha} = -(\nabla_j \mathcal{G}) \nabla_k \varphi_{\boldsymbol{x}}^\alpha \tag{A.4}$$

- Derivatives of component a_i of a vector $\boldsymbol{a}$ with respect to component a_j of the vector itself, with δ_{ij} as the Kronecker delta (*ij* component of the idemfactor $\boldsymbol{I}$):

$$\frac{\partial a_i}{\partial a_j} = \delta_{ij} \tag{A.5}$$

- Derivatives of component A_{ij} of a tensor with respect to component A_{kl} of the tensor itself:

$$\frac{\partial A_{ij}}{\partial A_{kl}} = \delta_{ik} \delta_{jl} \tag{A.6}$$

- Derivatives of the invariants of a dyadic with respect to the component of the dyadic itself (not necessarily symmetric):

$$\frac{\partial I_{\boldsymbol{A}}}{\partial A_{ij}} = \delta_{ij} \tag{A.7}$$

$$\frac{\partial II_{\boldsymbol{A}}}{\partial A_{ij}} \equiv \frac{1}{2}\frac{\partial}{\partial A_{ij}}\left[(\mathrm{Tr}\,\boldsymbol{A})^2 - \mathrm{Tr}\,(\boldsymbol{A}^2)\right] = I_{\boldsymbol{A}}\delta_{ij} - A_{ji} \tag{A.8}$$

$$\frac{\partial III_{\boldsymbol{A}}}{\partial A_{ij}} = A_{jk}A_{ki} - I_{\boldsymbol{A}}A_{ji} + II_{\boldsymbol{A}}\delta_{ij} = III_{\boldsymbol{A}}A_{ji}^{-1} \tag{A.9}$$

where $I_{\boldsymbol{A}} \equiv \mathrm{Tr}\,\boldsymbol{A} \equiv \boldsymbol{I} : \boldsymbol{A}$, and $III_{\boldsymbol{A}} \equiv \det \boldsymbol{A}$;

- Derivatives of the stress $\boldsymbol{T}$ with respect to position basis functions coefficients x_j^α:

$$\frac{\partial T_{ki}}{\partial x_j^\alpha} = -\eta_a\left[(\nabla_j v_i)\nabla_k\varphi_{\boldsymbol{x}}^\alpha + (\nabla_j v_k)\nabla_i\varphi_{\boldsymbol{x}}^\alpha\right] \tag{A.10}$$

- Derivatives of the stress $\boldsymbol{T}$ with respect to velocity basis functions coefficients v_j^α:

$$\frac{\partial T_{ki}}{\partial v_j^\alpha} = \eta_a\left(\delta_{ij}\nabla_k\varphi_{\boldsymbol{v}}^\alpha + \delta_{jk}\nabla_i\varphi_{\boldsymbol{v}}^\alpha\right) \tag{A.11}$$

- Derivatives of the elastic stress $\boldsymbol{\sigma}$ with respect to conformation $\boldsymbol{M}$:

$$\begin{aligned}\frac{\partial\sigma_{li}}{M_{jk}} ={}& 2\left(\frac{\partial\xi}{\partial M_{jk}} - \frac{\partial\zeta}{\partial M_{jk}}\right)\frac{\boldsymbol{M} : \boldsymbol{A}}{\boldsymbol{I} : \boldsymbol{M}}M_{li} - 2\frac{\xi-\zeta}{(\boldsymbol{I} : \boldsymbol{M})^2}\boldsymbol{A} : \boldsymbol{M}M_{li}\delta_{jk}\\ &+ 2\frac{\xi-\zeta}{\boldsymbol{I} : \boldsymbol{M}}\left(A_{kj}M_{li} + M_{pq}\frac{\partial A_{qp}}{\partial M_{jk}}M_{li} + \boldsymbol{M} : \boldsymbol{A}\delta_{jl}\delta_{ki}\right) + 2\frac{\partial\zeta}{\partial M_{jk}}M_{lp}A_{pi}\\ &+ 2\zeta\left(\delta_{jl}A_{ki} + M_{lp}\frac{\partial A_{pi}}{\partial M_{jk}}\right)\end{aligned} \tag{A.12}$$

where $\boldsymbol{A}$ is the derivative of the free energy with respect to conformation,

$$\boldsymbol{A} \equiv \frac{\partial a}{\partial\boldsymbol{M}} \tag{A.13}$$

$$\begin{aligned}A_{ij} \equiv \frac{\partial a}{\partial M_{ij}} &= \frac{\partial a}{\partial I_{\boldsymbol{M}}}\frac{\partial I_{\boldsymbol{M}}}{\partial M_{ij}} + \frac{\partial a}{\partial II_{\boldsymbol{M}}}\frac{\partial II_{\boldsymbol{M}}}{\partial M_{ij}} + \frac{\partial a}{\partial III_{\boldsymbol{M}}}\frac{\partial III_{\boldsymbol{M}}}{\partial M_{ij}}\\ &= \left(\frac{\partial a}{\partial I_{\boldsymbol{M}}} + \frac{\partial a}{\partial II_{\boldsymbol{M}}}\right)\delta_{ij} - \frac{\partial a}{\partial II_{\boldsymbol{M}}}M_{ji} + III_{\boldsymbol{M}}\frac{\partial a}{\partial III_{\boldsymbol{M}}}M_{ji}^{-1}\end{aligned} \tag{A.14}$$

Eqs. (A.1) and (A.14) hold in two- and three-dimensional flows.

A.1. Derivatives of the elliptic mesh generation equation

A.1.1. Derivatives with respect to position basis functions coefficients

$$\begin{aligned}\frac{\partial r_i^{\boldsymbol{x},\gamma}}{\partial x_j^\alpha} ={}& \int_{\Omega_0}\left(\nabla_k\varphi_{\boldsymbol{x}}^\alpha\nabla_j\psi_{\boldsymbol{x}}^\gamma\tilde{D}_{kl}K_{li}f - \nabla_k\psi_{\boldsymbol{x}}^\gamma\tilde{D}_{kl}K_{ji}\nabla_l\varphi_{\boldsymbol{x}}^\alpha f - \nabla_k\psi_{\boldsymbol{x}}^\gamma\tilde{D}_{kl}K_{li}\frac{\partial f}{\partial x_j^\alpha}\right)\mathrm{d}\Omega_0\\ &+ \text{boundary terms}\end{aligned} \tag{A.15}$$

A.2. Derivatives of the continuity equation

A.2.1. Derivatives with respect to position basis functions coefficients

$$\frac{\partial r^{c,\gamma}}{\partial x_j^\alpha} = \int_{\Omega_0} \psi_c^\gamma \left(\frac{\partial f}{\partial x_j^\alpha} \nabla \cdot \boldsymbol{v} - f \nabla_j v_i \nabla_i \varphi_{\boldsymbol{x}}^\alpha \right) \mathrm{d}\Omega_0 \tag{A.16}$$

A.2.2. Derivatives with respect to velocity basis functions coefficients

$$\frac{\partial r^{c,\gamma}}{\partial v_j^\alpha} = \int_{\Omega_0} \psi_c^\gamma \nabla_j \varphi_{\boldsymbol{v}}^\alpha f \, \mathrm{d}\Omega_0 \tag{A.17}$$

A.3. Derivatives of the momentum transport equation

A.3.1. Derivatives with respect to position basis functions coefficients

$$\begin{aligned} \frac{\partial r_i^{\boldsymbol{m},\gamma}}{\partial x_p^\alpha} = \int_{\Omega_0} \Bigg\{ & \frac{\partial f}{\partial x_p^\alpha} [\psi_{\boldsymbol{m}}^\gamma \rho (\boldsymbol{v} \cdot \nabla v_i - \nabla_i \Theta) + \nabla_k \psi_{\boldsymbol{m}}^\gamma T_{ki}] \\ & + f \left[-\psi_{\boldsymbol{m}}^\gamma \rho \boldsymbol{v} \cdot \nabla \varphi_{\boldsymbol{x}}^\alpha \nabla_p v_i - \nabla_p \psi_{\boldsymbol{m}}^\gamma \nabla_k \varphi_{\boldsymbol{x}}^\alpha T_{ki} + \nabla_k \psi_{\boldsymbol{m}}^\gamma \frac{\partial T_{ki}}{\partial x_p^\alpha} \right] \Bigg\} \mathrm{d}\Omega_0 \\ & + \text{boundary terms} \end{aligned} \tag{A.18}$$

A.3.2. Derivatives with respect to velocity basis functions coefficients

$$\frac{\partial r_i^{\boldsymbol{m},\gamma}}{\partial v_j^\alpha} = \int_{\Omega_0} \left[\psi_{\boldsymbol{m}}^\gamma \rho (\varphi_{\boldsymbol{v}}^\alpha \nabla_j v_i + \delta_{ij} \boldsymbol{v} \cdot \nabla \varphi_{\boldsymbol{v}}^\alpha) + \nabla_k \psi_{\boldsymbol{m}}^\gamma \frac{\partial T_{ki}}{\partial v_j^\alpha} \right] f \, \mathrm{d}\Omega_0 + \text{boundary terms} \tag{A.19}$$

A.3.3. Derivatives with respect to pressure basis functions coefficients

$$\frac{\partial r_i^{\boldsymbol{m},\gamma}}{\partial p^\alpha} = - \int_{\Omega_0} \nabla_i \psi_{\boldsymbol{m}}^\gamma \varphi_p^\alpha f \, \mathrm{d}\Omega_0 + \text{boundary terms} \tag{A.20}$$

A.3.4. Derivatives with respect to interpolated velocity gradient basis functions coefficients

$$\begin{aligned} \frac{\partial r_i^{\boldsymbol{m},\gamma}}{\partial L_{jk}^\alpha} = \int_{\Omega_0} & \varphi_{\boldsymbol{L}}^\alpha \left[(\mu - \eta_a)(\nabla_j \psi_{\boldsymbol{m}}^\gamma \delta_{ki} + \nabla_k \psi_{\boldsymbol{m}}^\gamma \delta_{ij}) + \nabla_l \psi_{\boldsymbol{m}}^\gamma \frac{\partial \eta_a}{\partial L_{jk}} (\nabla_l v_i - L_{li} + \nabla_i v_l - L_{il}) \right] f \mathrm{d}\Omega_0 \\ & + \text{boundary terms} \end{aligned} \tag{A.21}$$

A.3.5. Derivatives with respect to conformation basis functions coefficients

$$\begin{aligned} \frac{\partial r_i^{\boldsymbol{m},\gamma}}{\partial M_{jk}^\alpha} = - \int_{\Omega_0} & \varphi_{\boldsymbol{M}}^\alpha \nabla_l \psi_{\boldsymbol{m}}^\gamma \left[\frac{\partial \eta_a}{\partial M_{jk}} (\nabla_l v_i - L_{li} + \nabla_i v_l - L_{il}) + \frac{\partial \sigma_{li}}{\partial M_{jk}} \right] f \, \mathrm{d}\Omega_0 \\ & + \text{boundary terms} \end{aligned} \tag{A.22}$$

A.4. Derivatives of the velocity gradient interpolation equation

A.4.1. Derivatives with respect to position basis functions coefficients

$$\frac{\partial R_{ij}^{\boldsymbol{L},\alpha}}{\partial x_k^\gamma} = \int_{\Omega_0} \psi_{\boldsymbol{L}}^\alpha \left[\frac{\partial f}{\partial x_k^\alpha} \left(L_{ij} - \nabla_i \boldsymbol{v}_j + \frac{1}{\mathrm{Tr}\,\boldsymbol{I}} \nabla \cdot \boldsymbol{v} \delta_{ij} \right) + f \left(\nabla_i \varphi_{\boldsymbol{x}}^\gamma \nabla_k v_j - \frac{1}{\mathrm{Tr}\,\boldsymbol{I}} \nabla_p \varphi_{\boldsymbol{x}}^\gamma \nabla_k v_p \delta_{ij} \right) \right] \mathrm{d}\Omega_0 \tag{A.23}$$

A.4.2. Derivatives with respect to velocity basis functions coefficients

$$\frac{\partial R_{ij}^{\boldsymbol{L},\alpha}}{\partial v_k^\gamma} = \int_{\Omega_0} \psi_{\boldsymbol{L}}^\alpha \left(-\delta_{jk} \nabla_i \varphi_{\boldsymbol{v}}^\gamma + \frac{1}{\mathrm{Tr}\,\boldsymbol{I}} \nabla_k \varphi_{\boldsymbol{v}}^\gamma \delta_{ij} \right) f \, \mathrm{d}\Omega_0 \tag{A.24}$$

A.4.3. Derivatives with respect to interpolated velocity gradient basis functions coefficients

$$\frac{\partial R_{ij}^{\boldsymbol{L},\alpha}}{\partial L_{kl}^\gamma} = \int_{\Omega_0} \psi_{\boldsymbol{L}}^\alpha \delta_{ik} \delta_{jl} \varphi_{\boldsymbol{L}}^\gamma f \, \mathrm{d}\Omega_0 \tag{A.25}$$

A.5. Derivatives of the conformation transport equation

A.5.1. Derivatives with respect to position basis functions coefficients

$$\frac{\partial R_{ij}^{\boldsymbol{M},\gamma}}{\partial x_k^\alpha} = \int_{\Omega_0} \left\{ \left[\frac{\partial f}{\partial x_k^\alpha} \psi_{\boldsymbol{M}}^\gamma + f \left(\frac{\partial h}{\partial x_k^\alpha} \boldsymbol{v} \cdot \nabla \varphi_{\boldsymbol{M}}^\gamma - h \boldsymbol{v} \cdot \nabla \varphi_{\boldsymbol{x}}^\alpha \nabla_k \varphi_{\boldsymbol{M}}^\gamma \right) \right] \times \left(\boldsymbol{v} \cdot \nabla M_{ij} + P_{ij} + \frac{1}{\lambda} S_{ij} \right) - f \psi_{\boldsymbol{M}}^\gamma \boldsymbol{v} \cdot \nabla \varphi_{\boldsymbol{x}}^\alpha \nabla_k M_{ij} \right\} \mathrm{d}\Omega_0 \tag{A.26}$$

where

$$P_{ij} \equiv -2\xi \frac{\boldsymbol{D} : \boldsymbol{M}}{\boldsymbol{I} : \boldsymbol{M}} M_{ij} - \zeta \left(M_{il} D_{lj} + D_{il} M_{lj} - 2 \frac{\boldsymbol{D} : \boldsymbol{M}}{\boldsymbol{I} : \boldsymbol{M}} M_{ij} \right) - M_{il} W_{lj} - W_{li} M_{lj} \tag{A.27}$$

$$S_{ij} \equiv g_0 \delta_{ij} + g_1 M_{ij} + g_2 M_{il} M_{lj} \tag{A.28}$$

A.5.2. Derivatives with respect to velocity basis functions coefficients

$$\frac{\partial R_{ij}^{\boldsymbol{M},\gamma}}{\partial x_k^\alpha} = \int_{\Omega_0} \left[\psi_{\boldsymbol{M}}^\gamma \varphi_{\boldsymbol{v}}^\alpha \nabla_k M_{ij} + h \varphi_{\boldsymbol{v}}^\alpha \nabla_k \varphi_{\boldsymbol{M}}^\gamma \left(\boldsymbol{v} \cdot \nabla M_{ij} + P_{ij} + \frac{1}{\lambda} S_{ij} \right) \right] f \, \mathrm{d}\Omega_0 \tag{A.29}$$

A.5.3. Derivatives with respect to interpolated velocity gradient basis functions coefficients

$$\frac{\partial R_{ij}^{\boldsymbol{M},\gamma}}{\partial L_{kl}^\alpha} = \int_{\Omega_0} \psi_{\boldsymbol{M}}^\gamma \varphi_{\boldsymbol{L}}^\alpha \left[-(\xi - \zeta) \frac{M_{kl} + M_{lk}}{\boldsymbol{I} : \boldsymbol{M}} M_{ij} - \frac{1}{2} \zeta (M_{ik} \delta_{jl} + M_{il} \delta_{kj} + \delta_{ik} M_{lj} + \delta_{il} M_{kj}) - \frac{1}{2} (M_{ik} \delta_{jl} - M_{il} \delta_{jk} + \delta_{il} M_{kj} - \delta_{ik} M_{lj}) \right] f \, \mathrm{d}\Omega_0 \tag{A.30}$$

A.5.4. Derivatives with respect to conformation basis functions coefficients

$$\begin{aligned}\frac{\partial R_{ij}^{\boldsymbol{M},\gamma}}{\partial M_{kl}^{\alpha}} = \int_{\Omega_0} \psi_{\boldsymbol{M}}^{\gamma} \Bigg\{ & \boldsymbol{v}\cdot\nabla\varphi_{\boldsymbol{M}}^{\alpha}\delta_{ik}\delta_{jl} + \varphi_{\boldsymbol{M}}^{\alpha}\Bigg[-2\left(\frac{\partial\xi}{\partial M_{kl}} - \frac{\partial\zeta}{\partial M_{kl}}\right)\frac{\boldsymbol{D}:\boldsymbol{M}}{\boldsymbol{I}:\boldsymbol{M}}M_{ij} \\ & -2(\xi-\zeta)\left(\frac{D_{kl}}{\boldsymbol{I}:\boldsymbol{M}}M_{ij} - \frac{\boldsymbol{D}:\boldsymbol{M}}{(\boldsymbol{I}:\boldsymbol{M})^2}\delta_{kl}M_{ij} + \frac{\boldsymbol{D}:\boldsymbol{M}}{\boldsymbol{I}:\boldsymbol{M}}\delta_{ik}\delta_{jl}\right) \\ & -\frac{\partial\zeta}{\partial M_{kl}}(M_{ip}D_{pj} + D_{ip}M_{pj}) - \zeta(\delta_{ik}D_{lj} + D_{ik}\delta_{jl}) \\ & +\frac{1}{\lambda}\left(\frac{\partial g_0}{\partial M_{kl}}\delta_{ij} + \frac{\partial g_1}{\partial M_{kl}}M_{ij} + g_1\delta_{ik}\delta_{jl} + \frac{\partial g_2}{\partial M_{kl}}M_{ip}M_{pj} + g_2(\delta_{ik}M_{lj} + M_{ik}\delta_{jl})\right)\Bigg]\Bigg\}\, f\,\mathrm{d}\Omega_0 \end{aligned} \tag{A.31}$$

References

[1] K.N. Christodoulou, L.E. Scriven, Discretization of free surface flows and other moving boundary problems, J. Comp. Phys. 99 (1992) 39–55.

[2] V.F. deAlmeida, Gas–Liquid Counterflow Through Constricted Passages, Ph.D. thesis, University of Minnesota, Minneapolis, MN, 1995 (Available from UMI, Ann Arbor, MI, order number 9615160).

[3] P.A. Sackinger, P.R. Schunk, R.R. Rao, A Newton–Raphson pseudo-solid domain mapping technique for free and moving boundary problems: a finite element implementation, J. Comp. Phys. 125 (1996) 83–103.

[4] R. Guénette, M. Fortin, A new finite element method for computing viscoelastic flows, J. Non-Newtonian Fluid Mech. 60 (1995) 27–52.

[5] M.J. Szady, T.R. Salamon, A.W. Liu, R.C. Armstrong, R.A. Brown, A new mixed finite element method for viscoelastic flows governed by differential constitutive equations, J. Non-Newtonian Fluid Mech. 59 (1995) 215–243.

[6] M. Grmela, P.J. Carreau, Conformation tensor rheological models, J. Non-Newtonian Fluid Mech. 23 (1987) 271–294.

[7] A.N. Beris, B.J. Edwards, Thermodynamics of Flowing Systems with Internal Microstructure, 1st ed., Oxford University Press, Oxford, 1994.

[8] R.J.J. Jongschaap, K.H. deHaas, C.A.J. Damen, A generic matrix representation of configuration tensor rheological models, J. Rheol. 38 (1994) 769–796.

[9] M. Pasquali, Polymer Molecules in Free Surface Coating Flows, Ph.D. thesis, University of Minnesota, Minneapolis, MN, 2000 (Available from UMI, Ann Arbor, MI, order number 9963019).

[10] S.F. Kistler, L.E. Scriven, Coating flows, in: J.R.A. Pearson, S.M. Richardson (Eds.), Computational Analysis of Polymer Processing, Applied Science Publishers, London, 1983, pp. 243–299.

[11] S.F. Kistler, L.E. Scriven, Coating flow theory by finite element and asymptotic analysis of the Navier–Stokes system, Int. J. Numer. Methods Fluid. 4 (1984) 207–229.

[12] K.N. Christodoulou, Computational Physics of Slide Coating Flow, Ph.D. thesis, University of Minnesota, Minneapolis, MN, 1990 (Available from UMI, Ann Arbor, MI, order number 9021329).

[13] V.F. deAlmeida, Domain deformation mapping: application to variational mesh generation, SIAM J. Sci. Comput. 20 (1999) 1252–1275.

[14] M.S. Carvalho, Roll Coating Flows in Rigid and Deformable Gaps, Ph.D. thesis, University of Minnesota, Minneapolis, MN, 1996 (Available from UMI, Ann Arbor, MI, order number 9621887).

[15] M.S. Carvalho, L.E. Scriven, Flows in forward deformable roll coating gaps: comparison between spring and plane strain model of roll cover, J. Comp. Phys. 138 (1997) 449–479.

[16] M.S. Carvalho, L.E. Scriven, Three-dimensional stability analysis of free surface flows: application to forward deformable roll coating, J. Comp. Phys. 151 (1999) 534–562.

[17] F.P.T. Baaijens, Mixed finite element methods for viscoelastic flow analysis: a review, J. Non-Newtonian Fluid Mech. 79 (1998) 361–385.

[18] D. Rajagopalan, R.C. Armstrong, R.A. Brown, Finite element methods for calculation of steady, viscoelastic flows using constitutive equations with a Newtonian viscosity, J. Non-Newtonian Fluid Mech. 36 (1990) 159–192.

[19] J. Azaiez, R. Guénette, A. Aït-Kadi, Numerical simulation of viscoelastic flows through a planar contraction, J. Non-Newtonian Fluid Mech. 62 (1996) 253–277.

[20] Y.R. Fan, A comparative study of the discontinuous galerkin and continuous supg finite element methods for computation of viscoelastic flows, Comput. Methods Appl. Mech. Eng. 141 (1997) 47–65.

[21] J. Sun, M.D. Smith, R.C. Armstrong, R.A. Brown, Finite element method for viscoelastic flows based on the discrete adaptive viscoelastic stress splitting and the discontinuous galerkin method: Davss-g/dg, J. Non-Newtonian Fluid Mech. 86 (1999) 281–307.

[22] J.H. Bolstad, H.B. Keller, A multigrid continuation method for elliptic problems with folds, SIAM J. Sci. Stat. Comput. 7 (1985) 1081–1104.

[23] S.D.R. Wilson, The Taylor–Saffman problem for a non-Newtonian liquid, J. Fluid Mech. 220 (1990) 413–425.

[24] J.S. Ro, G.M. Homsy, Viscoelastic free surface flows: thin film hydrodynamics of Hele–Shaw and dip coating flows, J. Non-Newtonian Fluid Mech. 57 (1995) 203–225.

[25] J.J. Cai, Coating Rheology : Measurements, Modeling, and Applications, Ph.D. thesis, University of Minnesota, Minneapolis, MN, 1993 (Available from UMI, Ann Arbor, MI, order number 9517340).

[26] P. Dontula, Polymer Solutions in Coating Flows, Ph.D. thesis, University of Minnesota, Minneapolis, MN, 1999 (Available from UMI, Ann Arbor, MI, order number 9937847).

[27] S.F. Kistler, The Fluid Mechanics of Curtain Coating and Related Viscous Free Surface Flows with Contact Lines, Ph.D. thesis, University of Minnesota, Minneapolis, MN, 1983 (Available from UMI, Ann Arbor, MI, order number 8413795).

[28] J.M. deSantos, Two-Phase Cocurrent Downflow through Constricted Passages, Ph.D. thesis, University of Minnesota, Minneapolis, MN, 1991 (Available from UMI, Ann Arbor, MI, order number 9119386).

[29] D.F. Benjamin, Roll Coating Flows and Multiple Roll Systems, Ph.D. thesis, University of Minnesota, Minneapolis, MN, 1994 (Available from UMI, Ann Arbor, MI, order number 9512679).

[30] P.J. Flory, Principles of Polymer Chemistry, 1st ed., Cornell University Press, Ithaca, NY, 1953.

[31] M.D. Chilcott, J.M. Rallison, Creeping flow of dilute polymer solutions past cylinders and spheres, J. Non-Newtonian Fluid Mech. 29 (1988) 381–432.

[32] R.G. Larson, Convection and diffusion of polymer network strands, J. Non-Newtonian Fluid Mech. 13 (1983) 279–308.

[33] R.G. Larson, A constitutive equation for polymer melts based on partially extending strand convection, J. Rheol. 28 (1984) 545–571.

[34] G. Marrucci, N. Grizzuti, The free energy function of the Doi–Edwards theory: analysis of the instabilities in stress relaxation, J. Rheol. 27 (1983) 433–450.

[35] M. Doi, S.F. Edwards, The Theory of Polymer Dynamics, 1st ed., Oxford University Press, Oxford, 1986.

[36] R.G. Larson, Constitutive Equations for Polymer Melts and Solutions, 1st ed., Butterworths, Boston, 1988.

[37] M. Renardy, W.J. Hrusa, J.A. Nohel, Mathematical Problems in Viscoelasticity, Wiley, New York, 1987.

[38] J. Vander Zanden, M. Hulsen, Mathematical and physical requirements for successful computations with viscoelastic fluid models, J. Non-Newtonian Fluid Mech. 29 (1988) 93–117.

[39] C. Truesdell, W. Noll, The non-linear field theories of mechanics, in: S. Flügge (Ed.), Encyclopedia of Physics, vol. III/3, 1st ed., Springer, Berlin, 1965.

[40] W.R. Hamilton, On quaternions, Proc. R. Ir. Acad. 3 (1847) 273–292.

[41] W.R. Hamilton, On quaternions, or on a new system of imaginaries in algebra, Philos. Mag. Ser. 3 31 (1847) 278–293.

[42] M.J. Crowe, A History of Vector Analysis, Dover, New York, 1994 (Originally published by University of Notre Dame Press, 1967).

[43] I.S. Duff, A.M. Erisman, J.K. Reid, Direct Methods for Sparse Matrices, 1st ed., Oxford University Press, Oxford, 1989.

[44] R.A. Bird, R.C. Armstrong, O. Hassager, Dynamics of Polymeric Liquids, vol. 1, 2nd ed., Wiley, New York, 1987.

[45] P.R. Schunk, L.E. Scriven, Constitutive equations for modeling mixed extension and shear in polymer solution processing, J. Rheol. 34 (1990) 1085–1119.

[46] L.E. Wedgewood, K.R. Geurts, A non-affine network model for polymer melts, Rheol. Acta 33 (1995) 369–384.

[47] O.H. Faxén, Forces exerted on a rigid cylinder in a viscous fluid between two parallel fixed planes, Ingenjörsvetenskapsakad. Handl. 187 (1946) 1–13 (English equivalent: R. Swed. Acad. Eng. Sci. Proc.).

[48] W.J. Silliman, Viscous Film Flows with Contact Lines: Finite Element Simulation, A Basis for Stability Assessment and Design Optimization, Ph.D. thesis, University of Minnesota, Minneapolis, MN, 1979 (Available from UMI, Ann Arbor, MI, order number 7926172).

[49] T.T. Perkins, S.R. Quake, D.E. Smith, S. Chu, Relaxation of a single polymer molecule observed by optical microscopy, Science 264 (1994) 822–826.

[50] H.P. Babcock, D.E. Smith, J.S. Hur, E.S.G. Shaqfeh, S. Chu, Relating the microscopic and macroscopic response of a polymeric fluid in a shearing flow, Phys. Rev. Lett. 85 (2000) 2018–2021.

[51] S. Richardson, A 'stick-slip' problem related to the motion of viscous liquid in a corner, Proc. Cambridge Phil. Soc. 67 (1970) 477.

[52] T.R. Salamon, D.E. Bornside, R.C. Armstrong, R.A. Brown, The role of surface tension in the dominant balance in the die swell singularity, Phys. Fluids 7 (1995) 2328–2344.

[53] T.R. Salamon, D.E. Bornside, R.C. Armstrong, R.A. Brown, Local similarity solutions in the presence of a slip boundary condition, Phys. Fluids 9 (1997) 1235–1247.

[54] T.R. Salamon, D.E. Bornside, R.C. Armstrong, R.A. Brown, Local similarity solutions for the stress field of an Oldroyd-B fluid in the partial-slip/slip flow, Phys. Fluids 9 (1997) 2191–2209.

[55] C.W. Macosko, Rheology, 1st ed., VCH, New York, 1994.

[56] W.W. Graessley, Polymer chain dimensions and the dependence of viscoelastic properties on concentration, molecular weight and solvent power, Polymer 21 (1980) 258–262.

[57] C.N. Aggelidis, M. Pasquali, L.E. Scriven, Calendering: rheology, computations, and experiments, in: D.M. Binding, N.E. Hudson, J. Mewis, J.-M. Piau, C.J.S. Petrie, P. Townsend, M.H. Wagner, K.Walters (Eds.), Proceedings of the XIIIth International Congress on Rheology, vol. 3, Cambridge, UK, 2000, pp. 425–427.

[58] E.C. Lee, M.J. Solomon, S.J. Muller, Molecular orientation and deformation of polymer solutions under shear: a flow light scattering study, Macromolecules 30 (1997) 7313–7321.

[59] P. LeDuc, C. Haber, G. Bao, D. Wirtz, Dynamics of individual flexible polymers in a shear flow, Nature 399 (1999) 564–566.